TÜBİTAK

Turkish Journal of Earth Sciences

http://journals.tubitak.gov.tr/earth/

Research Article

Turkish J Earth Sci
(2015) 24: 529-565

doi:10.3906/yer-1503-8

Assessment of seismic hazard in the Erzincan (Turkey) region: construction of local velocity models and evaluation of potential ground motions

Ayşegül ASKAN[1,*], Shaghayegh KARIMZADEH[1], Michael ASTEN[2], Nazan KILIÇ[3], Fatma Nurten ŞİŞMAN[4], Cenk ERKMEN[3]

[1]Department of Civil Engineering, Middle East Technical University, Ankara, Turkey
[2]School of Earth Atmosphere and Environment, Monash University, Melbourne, Australia
[3]Earthquake Department, Prime Ministry Disaster and Emergency Management Authority, Ankara, Turkey
[4]Department of Engineering Sciences, Middle East Technical University, Ankara, Turkey

Received: 05.03.2015 • **Accepted/Published Online:** 10.09.2015 • **Printed:** 30.11.2015

Abstract: The fundamental step in estimation of seismic damage and losses in urban areas is identification of regional potential seismic hazard. The accuracy of seismic analyses depends on the reliability of the local input parameters used in the corresponding hazard and loss models. This paper presents detailed seismic hazard analyses for an earthquake-prone region using locally derived source and site parameters. Main components of this study are construction of local seismic velocity models, probabilistic and deterministic seismic hazard analyses, and estimation of corresponding potential ground motions. The study area is Erzincan, which is a city on the eastern part of the North Anatolian Fault Zone. Located at a triple junction of major fault systems within a basin structure, Erzincan experienced major events (Ms ~8.0) in 1939 and (Mw = 6.6) in 1992. This study presents the first discussion in the literature on site-specific probabilistic and deterministic hazard analyses for Erzincan. Using locally derived input parameters in site response modeling and hazard analyses, the earthquake potential of Erzincan is investigated in detail. Probabilistic seismic hazard analyses with a hybrid source model composed mainly of line sources show that for a return period of 475 years, the maximum peak ground acceleration value in the Erzincan city center is computed to be almost 1 *g*. On the other hand, probabilistic hazard analyses with only area sources yield ground motion amplitudes that are almost half of those obtained by the hybrid model. The deterministic hazard analyses also show that peak ground acceleration in the city center for a scenario event of Mw = 7.0 reaches 1.25 *g* at a soft soil site located at 2 km in distance from the fault plane. In summary, numerical results obtained with locally derived input parameters indicate that Erzincan has significant potential for hazard in terms of both local earthquake occurrence and site amplifications.

Key words: Erzincan, microtremor array analysis, velocity model, stochastic finite fault method, deterministic seismic hazard analysis, probabilistic seismic hazard analysis

1. Introduction

Study of regional seismicity in seismically active areas is significant for many disciplines varying from earth sciences to earthquake engineering. Regional seismicity broadly includes the nature, size, and frequency of earthquakes in a selected region. Such regional information is employed for many purposes including seismic hazard analyses, wave propagation models, and seismic damage and loss estimations. Past data are mostly collected in the form of earthquake catalogs and the corresponding ground motion datasets. These datasets are used for evaluation of seismicity in any region of interest. However, for seismic loss mitigation and disaster planning purposes, it is also important to assess potential earthquakes and the corresponding ground motions in earthquake-prone areas.

The main step in the assessment of seismic hazard in any region is to perform an analysis of seismicity. Seismic hazard analyses can be performed either in a probabilistic or deterministic framework (e.g., Cornell, 1968; Frankel, 1993; Olsen et al., 1996; McGuire, 2004). These analyses have become very popular recently and are employed for many seismically active areas all over the world. However, for accurate and reliable results, the source and path (wave propagation) parameters should be studied carefully at the regional level (Askan et al., 2013). This requires a detailed study of the existing sources in the region of interest and its vicinity as well as seismic velocity models of soil structure, which directly affect the ground motion amplitudes.

In this study, initially local S-wave velocity models are constructed for the study area by forming one-dimensional

* Correspondence: aaskan@metu.edu.tr

soil velocity profiles at several sites. Previously, regional velocity models were derived for the Erzincan region (Aktar et al., 2004; Kaypak, 2008); however, local models are also necessary since the hazard analyses use local velocity information to yield ground motion amplitudes. To derive these local models, a passive seismic method that uses microtremors is employed. Microtremor array techniques have been used effectively in the past (e.g., Birgören et al., 2009; Kocaoğlu and Fırtana, 2011; Sisman et al., 2013). In this study, the multimode spatial autocorrelation (MMSPAC) method introduced by Asten (2004) and Roberts and Asten (2004) is employed. The MMSPAC method is fundamentally a development from the original spatial autocorrelation method (SPAC) introduced by Aki (1957). Both probabilistic and deterministic analyses are then performed to assess potential seismicity and ground motion distribution. Erzincan, a city located in eastern Turkey, is selected as the study region since the eastern segments of the North Anatolian Fault Zone (NAFZ) are relatively less studied when compared to the western parts. In addition, the eastern segments are much more sparsely monitored; for instance, the 1992 Erzincan earthquake (Mw = 6.6) was recorded by only 3 stations within an epicentral distance of 200 km even though the city center is located at the intersection of three main fault systems. Thus, it is important to assess the seismic hazard around Erzincan through comprehensive hazard analyses.

2. Study area

Erzincan is considered to be one of the most hazardous regions of the world in terms of earthquake occurrences. Historical records evidence 18 large (M > 8) earthquakes in the close vicinity of Erzincan within the past 1000 years (Barka, 1993). The Erzincan city center is located at the intersection of three active fault zones, namely the NAFZ, North East Anatolian Fault Zone (NEAFZ), and Ovacık Fault. These fault zones characterize the basic seismotectonics of the region. The NAFZ displays right-lateral strike-slip faulting whereas the EAFZ and NEAFZ have left-lateral strike-slip faulting. The city center is built on an alluvium pull-apart basin with dimensions of 50 km × 15 km that is formed as a result of the tectonic interactions in the region.

In the last century, Erzincan experienced two destructive earthquakes due to activity on the NAFZ. The first one was the 1939 earthquake (Ms ~8.0) that caused severe structural damage leading to more than 30,000 fatalities. The latter was the 1992 earthquake (Mw = 6.6) that led to major structural damage in the city center, resulting in an economic loss of 3–5 million US dollars and approximately 500 fatalities (Lav et al., 1993; Akinci et al., 2001). The epicenters of these earthquakes as well as the corresponding faults and source mechanisms are displayed in Figure 1. The other faults in the region that are used in the hazard analyses will be presented in Section 4 in detail.

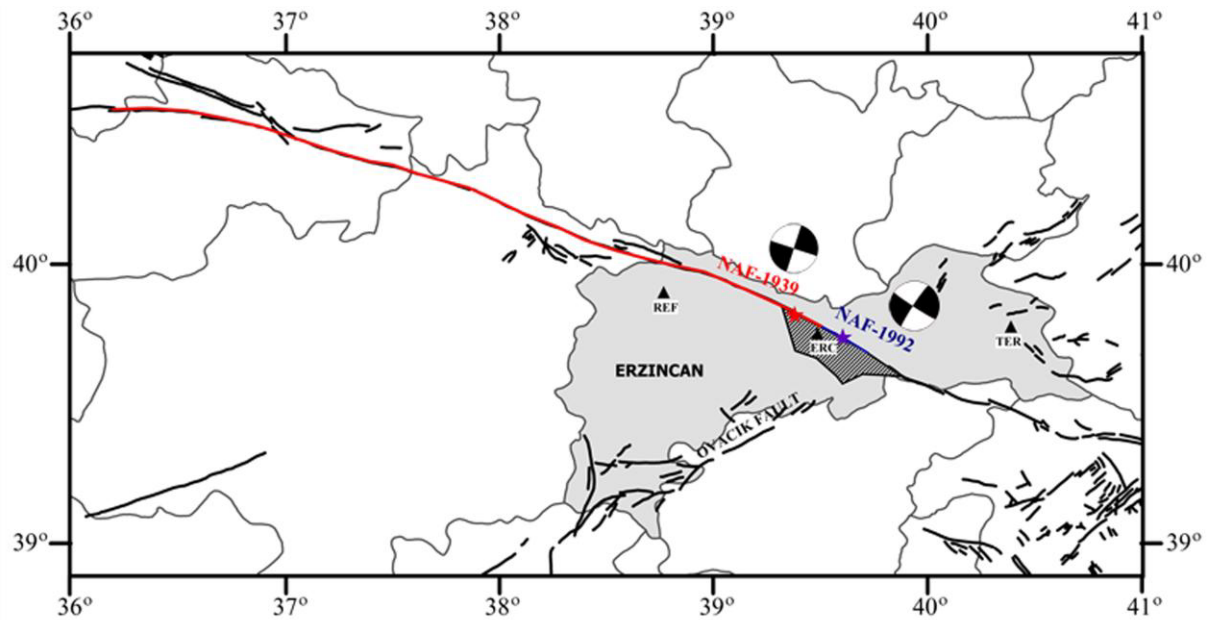

Figure 1. Seismotectonics in the Erzincan region with the fault systems (red curve: causative fault of the 1939 earthquake, blue curve: causative fault of the 1992 earthquake) along with the epicenters (shown with stars) and focal mechanisms of the 1939 and 1992 earthquakes (after Askan et al., 2013). The light gray polygon represents Erzincan Province boundaries while the smaller dark gray polygon shows the Erzincan basin.

The intense seismic activity in addition to the sparse strong ground motion station network in the region as well as lack of detailed studies make the area suitable for the detailed regional analyses presented in this paper.

3. Construction of the soil model

In this section, S-wave velocity profiles at nine sites selected in the Erzincan basin are studied with the microtremor method (Figure 2). The locations of these sites are selected in particular to form arrays in the east-west and north-south directions. In the subsequent sections, initially the methodology is described, and then the applications and the results at selected sites are presented.

3.1. MMSPAC methodology

In this study, a passive seismic method is performed to obtain the one-dimensional S-wave velocity profile (Vs) of the upper 100 m of sediments. The method used here employs array-based measurement of seismic noise (microtremors) of cultural origin above 1 Hz and measures Rayleigh-wave velocity dispersion. MMSPAC is employed herein as described by Asten et al. (2004, 2014) and Asten (2006), which is a development from the original SPAC introduced by Aki (1957).

Aki (1957), Okada (2003), and several other authors who performed the SPAC method calculated the coherency spectrum and then inverted the phase velocity dispersion curve. These authors fit the modeled and observed phase velocity dispersion curves to estimate the S-wave velocity profile at a site of interest.

Alternative approaches to the SPAC method were introduced previously in several studies, such as those of Asten et al. (2004), Roberts and Asten (2004), Wathelet et al. (2005), Asten (2006), and Kocaoğlu and Fırtana (2011). The goal of these alternative approaches is to fit the observed SPAC spectra directly to modeled SPAC spectra. In other words, the dispersion curve is not directly inverted but is rather obtained as a by-product after fitting the observed and modeled SPAC curves. Fundamental advantages of the MMSPAC method are that it facilitates identification of the higher mode surface wave energy if present (Asten et al., 2004), mitigates Vs bias by avoiding the intermediate and highly nonlinear process of calculating Rayleigh-wave phase velocities from observed data, and facilitates use of SPAC curves on secondary peaks and troughs of the Bessel function shown in Eq. (1). For example, if incoherent noise is present in the SPAC spectrum, this causes a reduction in the magnitude of SPAC values and a consequent biasing towards lower velocities of phase velocity estimates derived from the SPAC. Use of secondary peaks and troughs of the Bessel function for extraction of phase velocities is difficult due to the inverse Bessel function being multivalued. Direct fitting of observed and modeled SPAC curves removes this ambiguity and extends the useable frequency range for a given array typically by a factor of two to five (Asten, 2009).

The MMSPAC method is performed by fitting observed and model SPAC data through the following relation:

$$c_m(f) = J_0\left[2\pi f r / C_p(f)\right], \quad (1)$$

where $c_m(f)$ is the modeled spatially averaged coherency, f is frequency, r is the station separation (Figure 3a), and $c_p(f)$ is the modeled phase velocity for a layered earth. A centered equilateral triangular array of four stations allows measurement of SPAC at two station separations, being the radius r_1 and the side length r_2, and from geometry (Figure 3a):

$$r_2 = r_1 \times \sqrt{3}. \quad (2)$$

On the other hand, Figure 3b shows the recording instruments, which are Guralp CMG-6TD seismometers. These seismometers are ultralight-weight digital three-axis instruments with three sensors that can record the north-south, east-west, and vertical components of ground motion. Sensors are sensitive to ground motions over a frequency range of 0.033–50 Hz (http://www.guralp.com/documents/MAN-T60-0002.pdf). The instrument has a built-in 24-bit digitizer, GPS sensor, and crystal clock synchronizable with a GPS signal.

Asten (2006, Appendix A) is followed for the data processing: first, data segments of typical length of 20 min are selected from total recording times of about 60 min. Only vertical-component data at the center G and stations of A, B, and C of a triangular array (Figure 3a) are employed. Each data length is first weighted with a Hanning bell fader, then transformed to a complex spectrum by a discrete Fourier transform on a data length of n points, sampled at spacing $\Delta t = 0.001$ *sec*. The complex coherency spectrum for every possible pair of stations is computed using frequency averaging, in windows of width 39 Δf, where $\Delta f = 1 / (n \times \Delta t)$ is the sample interval of the digital spectrum and is set by the length of the selected time series. A triangular array of side-length L allows spatial averaging of coherencies (SPAC) using station pairs GA, GB, and GC (interstation spacing $L / \sqrt{3}$) and using station pairs AB, BC, and CA (interstation spacing L). The two observed SPAC spectra are fitted simultaneously with model SPAC spectra in the interpretation process. The fitting process utilizes iterative forward modeling with a least-squares criterion for best fit of a layered earth model, over some chosen range of frequencies. Sensitivities of relevant parameters (layer thicknesses and shear-wave velocities Vs) may be derived using the methods described by Asten et al. (2014) but are not utilized in this hazard study.

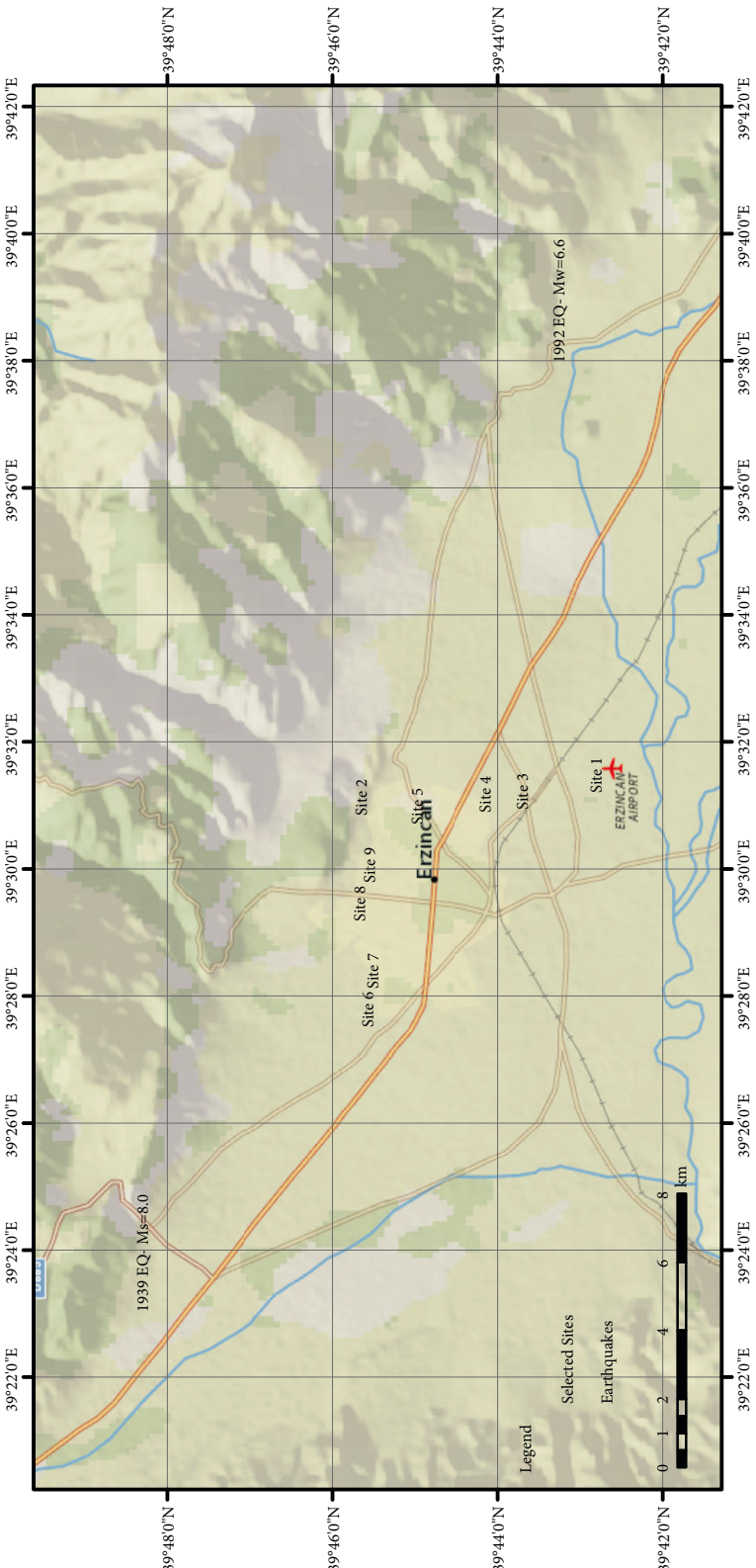

Figure 2. Location of the selected sites in Erzincan basin (the blue curve is the Fırat (Euphrates) river, the orange curve is the highway, and the gray curves show the avenues in the city center).

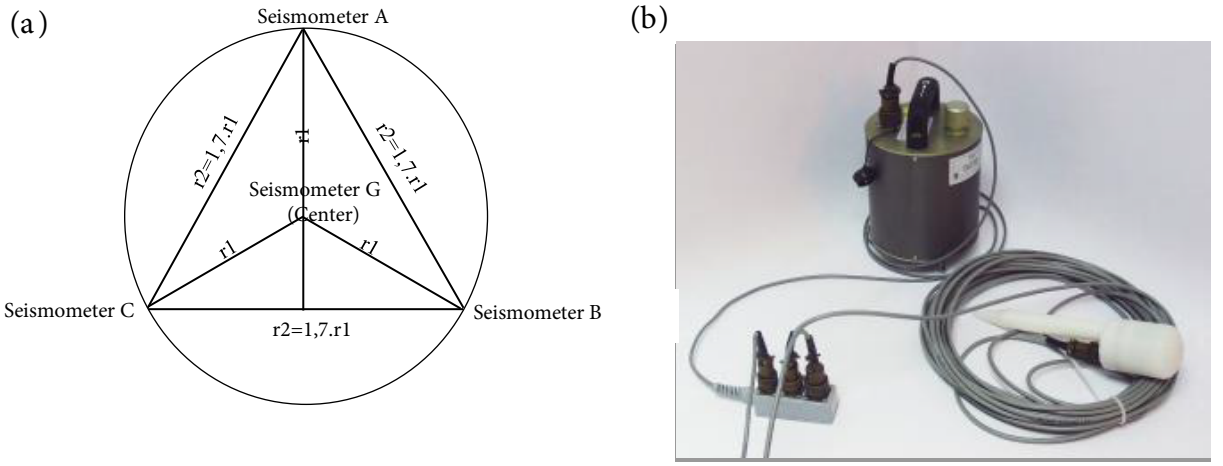

Figure 3. (a) General form of the array geometry and (b) recording instrument used in the field.

In addition, three-component data at the array center are collected in order to make use of horizontal to vertical particle motion ratio (HVSR) spectra. HVSR methods can be used in inversion schemes in combination with SPAC data (e.g., Arai and Tokimatsu, 2004, 2005; Picozzi and Albarello, 2007; Hayashi et al., 2011; Ikeda et al., 2013). In this study, a simpler approach is used whereby in addition to the quantitative fitting of SPAC curves, peak frequencies of observed and modeled HVSR curves are matched to constrain depth of deep interfaces. As noted by Asten et al. (2014) and Hayashi et al. (2011), it is common to find that the useful frequency range of HVSR data extends to lower frequencies than do SPAC data, and this feature is also evident in data analyzed in this paper. Quantitative use of HVSR data suffers from complications as horizontal surface wave energy contains Love waves in addition to the Rayleigh waves considered in the analysis. Bonnefoy-Claudet et al. (2006, 2008) reviewed instances where estimation of the ratio of Love to Rayleigh wave energy was obtained and noted a range of between 50% and 85% energy in Love waves, which has the effect of offsetting observed HVSR curves to higher ratios than would be expected if energy were restricted to Rayleigh waves alone. A further complication of the HVSR method is that a temporary seismic station placed on a pavement or shallow hole may be subject to wind noise (even when shielded in the field). Wind noise may produce rocking of the seismometer, which adds energy to the horizontal seismic components. For these wave propagation and logistical reasons, the frequency of peaks in HVSR is the parameter of most interest, since it is this frequency rather than absolute HVSR amplitude that is most sensitive to the depth to, and shear-wave velocity above, significant layer boundaries.

Two prior applications to other basins on the NAFZ of HVSR methodology supplementing SPAC interpretations were described by Sisman et al. (2013) and Asten et al. (2014).

3.2. Applications at 9 sites and one-dimensional (1D) velocity models

The MMSPAC method as outlined previously is applied to the data collected at the 9 sites shown in Figure 2. The locations of the sites are selected such that they form arrays in the east-west and north-south directions. The geometry of stations at each site is presented in Figure 4. At some sites, due to the urban arrangements, different geometries and lengths of arrays are used.

The coherency curves at all sites for distances r_1 and r_2 along with the HVSR curves and the velocity profiles obtained with joint use of SPAC and HVSR data are demonstrated in Figures 5–13. HVSR curves display the mean HVSR and ±1 standard error of the mean values to show the associated variations and uncertainty. In Figures 5–13, 1D velocity models at all sites down to 400 m as well as a close view of the top 30 m are presented. In cases where SPAC and HVSR data are not consistent, SPAC data, which are interpreted by quantitative methods and use only vertical-component energy, are favored. It is noted that poorer correspondence of SPAC and HVSR models occurs on the east-west arm of the survey, nearer to the northern slopes of the basin where reduced accuracy may be expected due to departures from the idealized layered-earth models.

An important parameter to identify local soil conditions at any site is Vs30, which is defined as the 30-m average shear wave velocity in units of m/s. It is used frequently in engineering seismology and earthquake engineering fields. Table 1 displays the Vs30 values at the 9 sites of interest. It is observed that the northern regions (Sites 2 and 8) are quite stiff while the southern areas near the

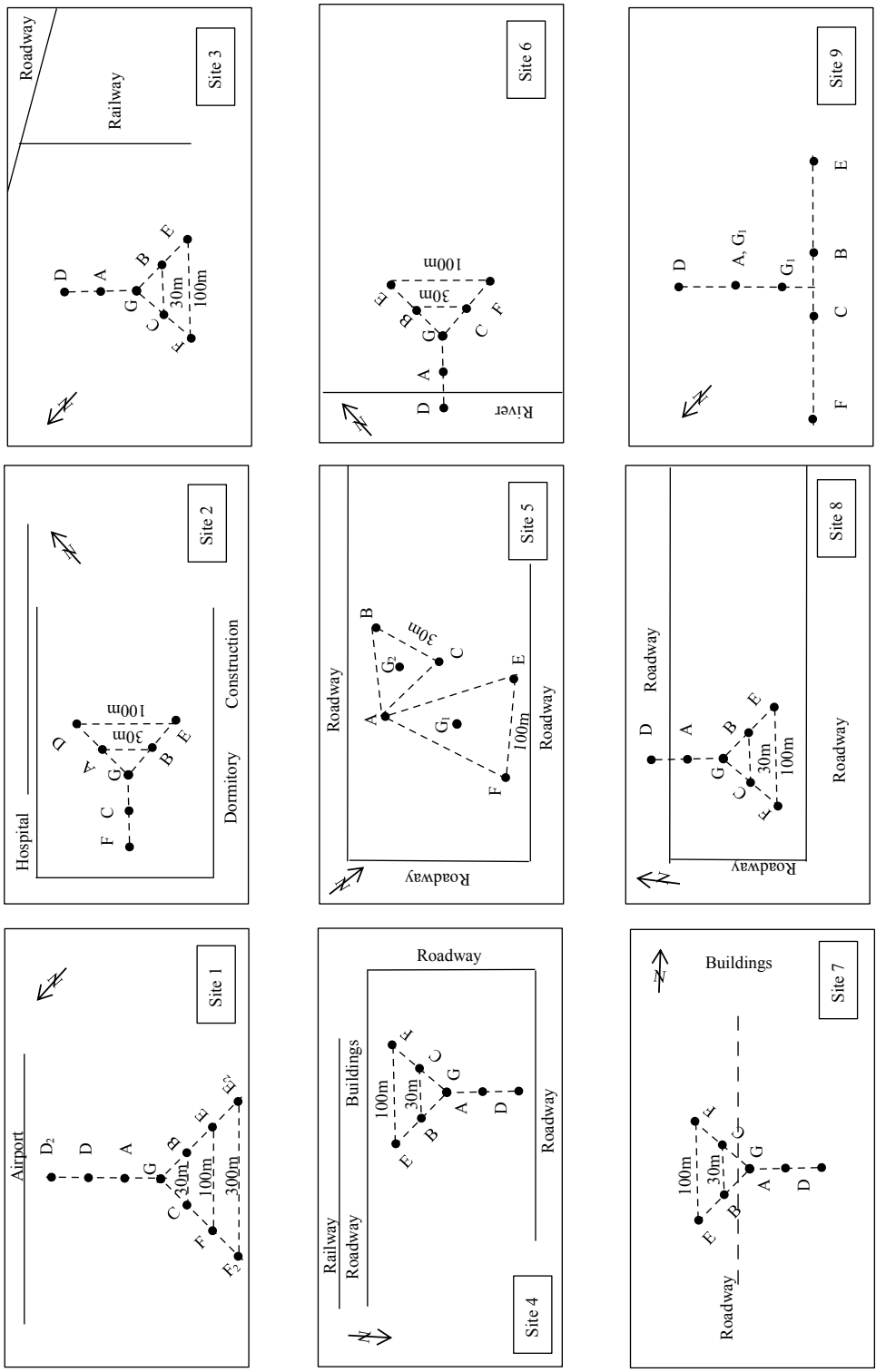

Figure 4. Sketch map of arrays at the 9 sites of interest.

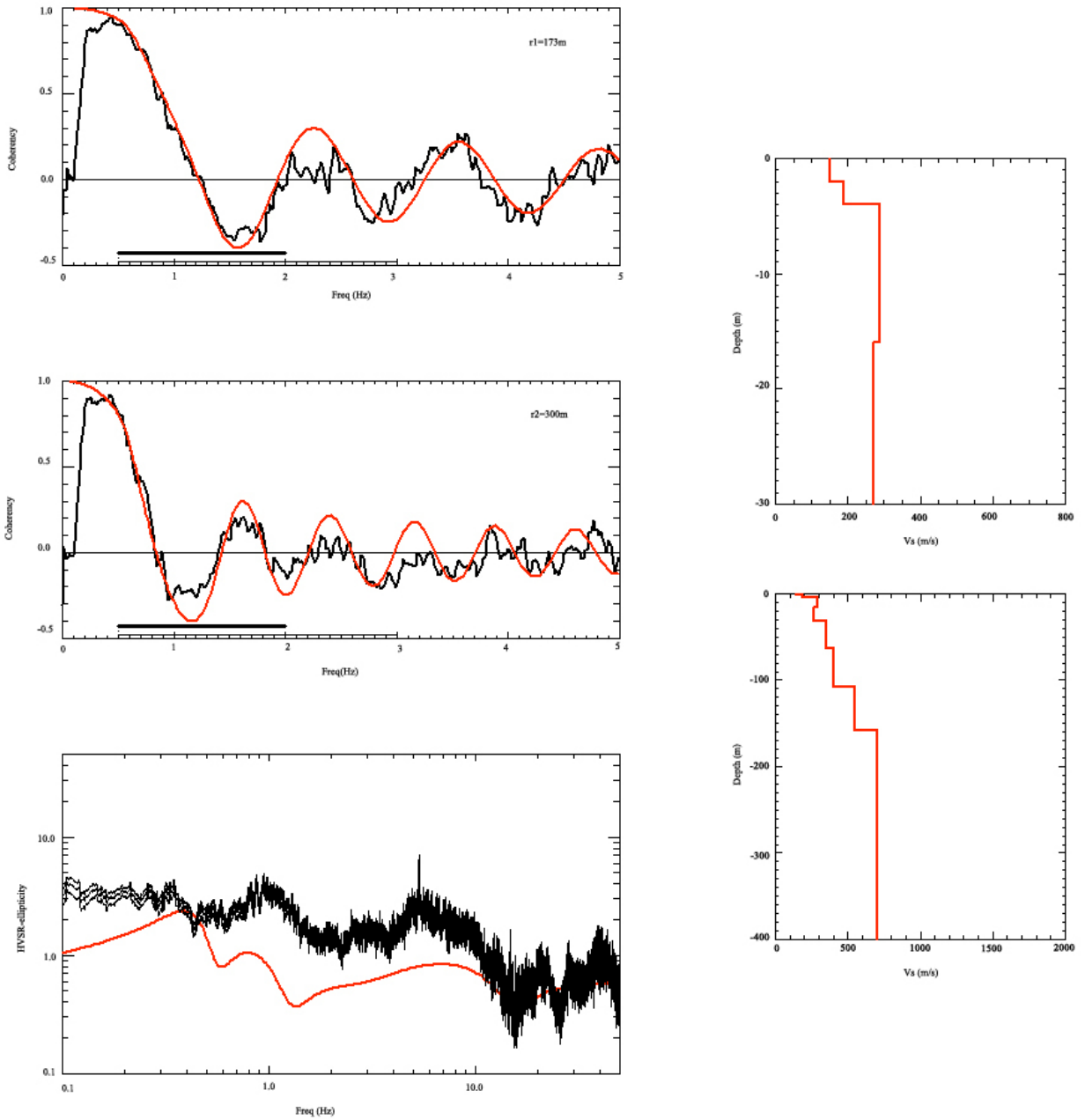

Figure 5. Left column: Coherency curves at Site 1 for station separations of r1 and r2 and HVSR curve. In SPAC curves, black is the observed spectra and red is the fitted model SPAC for the Rayleigh fundamental mode. In the HVSR curve, black is the observed spectra and red is the modeled ellipticity curve. Right column: 1D shear wave velocity profiles down to 30 m (top panel) and 400 m depth (bottom panel).

Erzincan airport (Site 1) are located on softer soil deposits. The basin structure is obvious when one compares the distribution of Vs30 values in the north-south and east-west directions (Figures 5–13 and Table 1).

4. Probabilistic seismic hazard analyses

Hazard analysis that takes into account the inherent uncertainties involved in earthquake occurrences (location, magnitude, frequency of occurrence, etc.) within a probabilistic framework is called probabilistic seismic hazard analysis (PSHA). The purpose of PSHA is to identify the probabilities of exceedance of certain ground motion levels in a given period of time at a selected site of interest by considering all probable earthquakes. The method was originally developed by Cornell (1968) and has since become very popular worldwide. In this

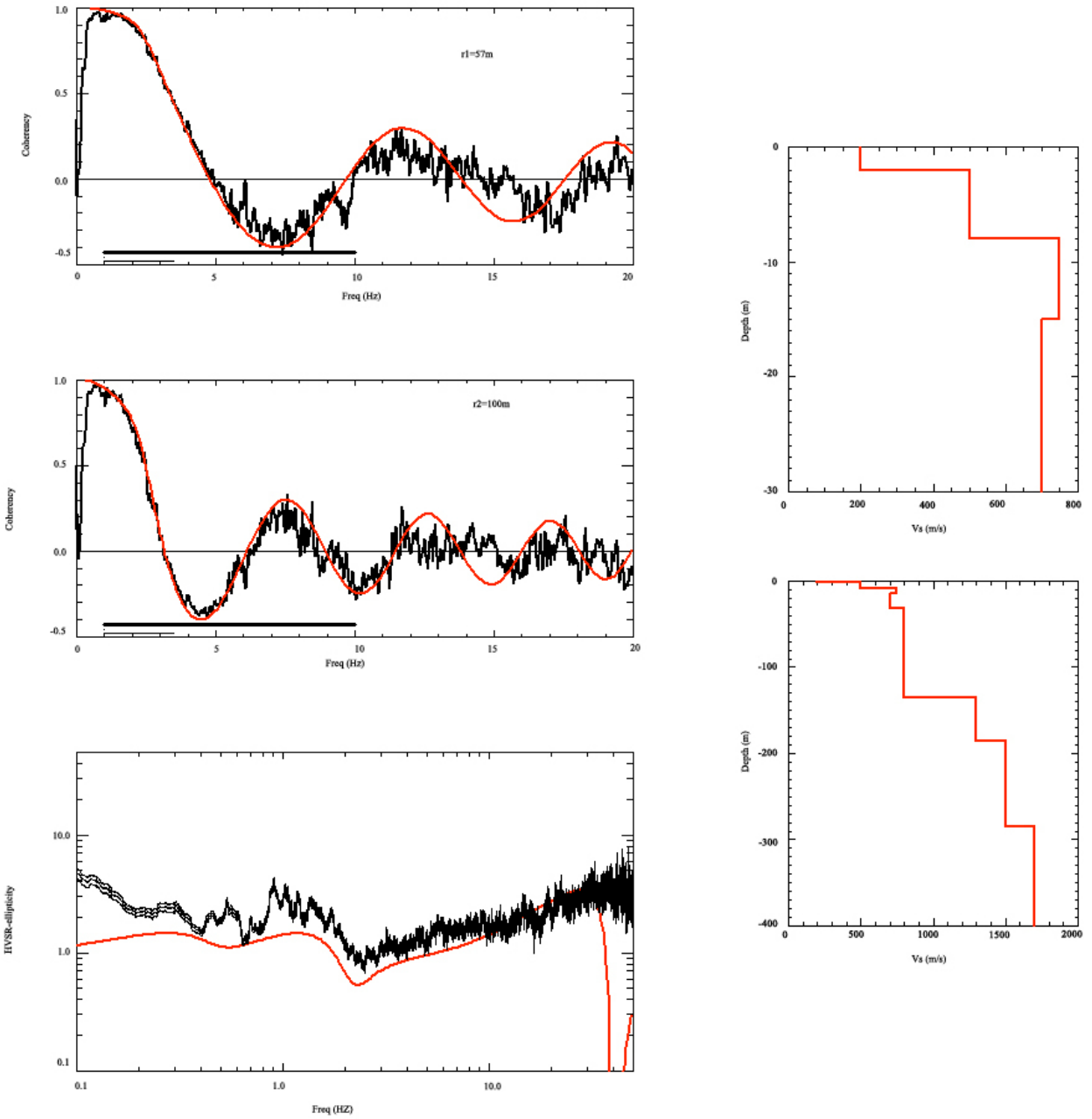

Figure 6. Left column: Coherency curves at Site 2 for station separations of r1 and r2 and HVSR curve. In SPAC curves black is the observed spectra and red is the fitted model SPAC for the Rayleigh fundamental mode. In the HVSR curve, black is the observed spectra and red is the modeled ellipticity curve. Right column: 1D shear wave velocity profiles down to 30 m (top panel) and 400 m depth (bottom panel).

paper, PSHA is performed in the Erzincan region at the 9 selected sites using local seismic sources and local site information in the form of Vs30 values derived from the 1D wave velocity models constructed in this study.

4.1. Methodology for PSHA

The fundamental steps of PSHA are summarized in the form of a flowchart in Figure 14. Identifying the seismic sources that remain within a region of interest and its vicinity is considered as the first step in seismic hazard analysis. Geological, geophysical, and seismological data as well as seismicity maps that show the epicenters of past earthquakes are utilized to determine the geographical locations of the seismic sources. There are three main types of seismic source models: point, fault (line), and area

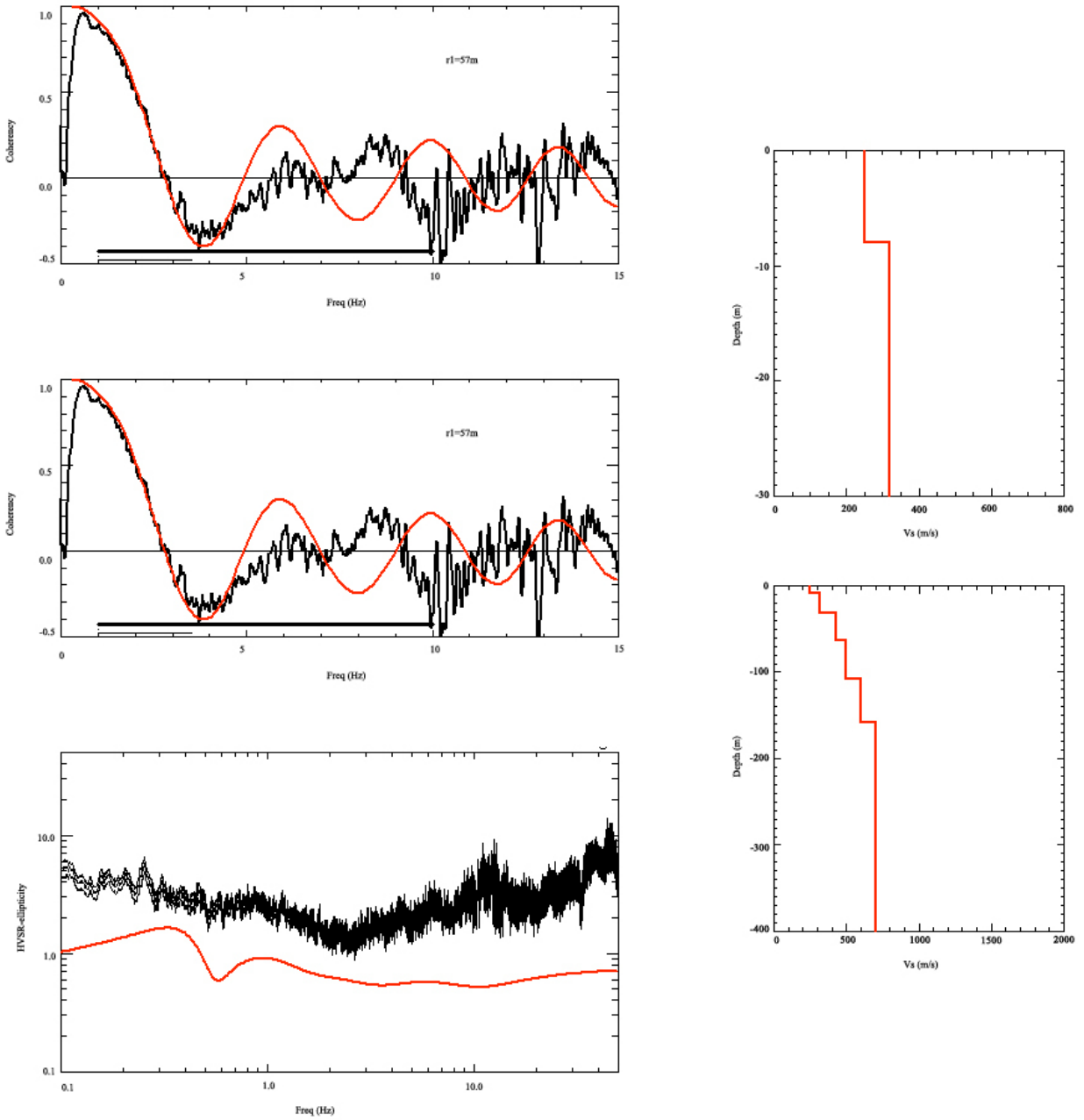

Figure 7. Left column: Coherency curves at Site 3 for station separations of r1 and r2 and HVSR curve. In SPAC crves black is the observed spectra and red is the fitted model SPAC for the Rayleigh fundamental mode. In the HVSR curve, black is the observed spectra and red is the modeled ellipticity curve. Right column: 1D shear wave velocity profiles down to 30 m (top panel) and 400 m depth (bottom panel).

source models. In this study, line and area source models are employed.

The next step after determining the seismic sources is to create a magnitude-frequency relationship for each source in the region. In the classical PSHA model developed by Cornell (1968), earthquake magnitude is assumed to be exponentially distributed based on the linear magnitude-recurrence relationship recommended by Richter (1958). Schwartz and Coppersmith (1984) indicated that the exponentially distributed magnitude models represent the earthquake magnitudes quite well in a large region but may underestimate the recurrence rate of large earthquakes on individual fault segments and proposed the characteristic earthquake model. Later, Youngs and Coppersmith (1985)

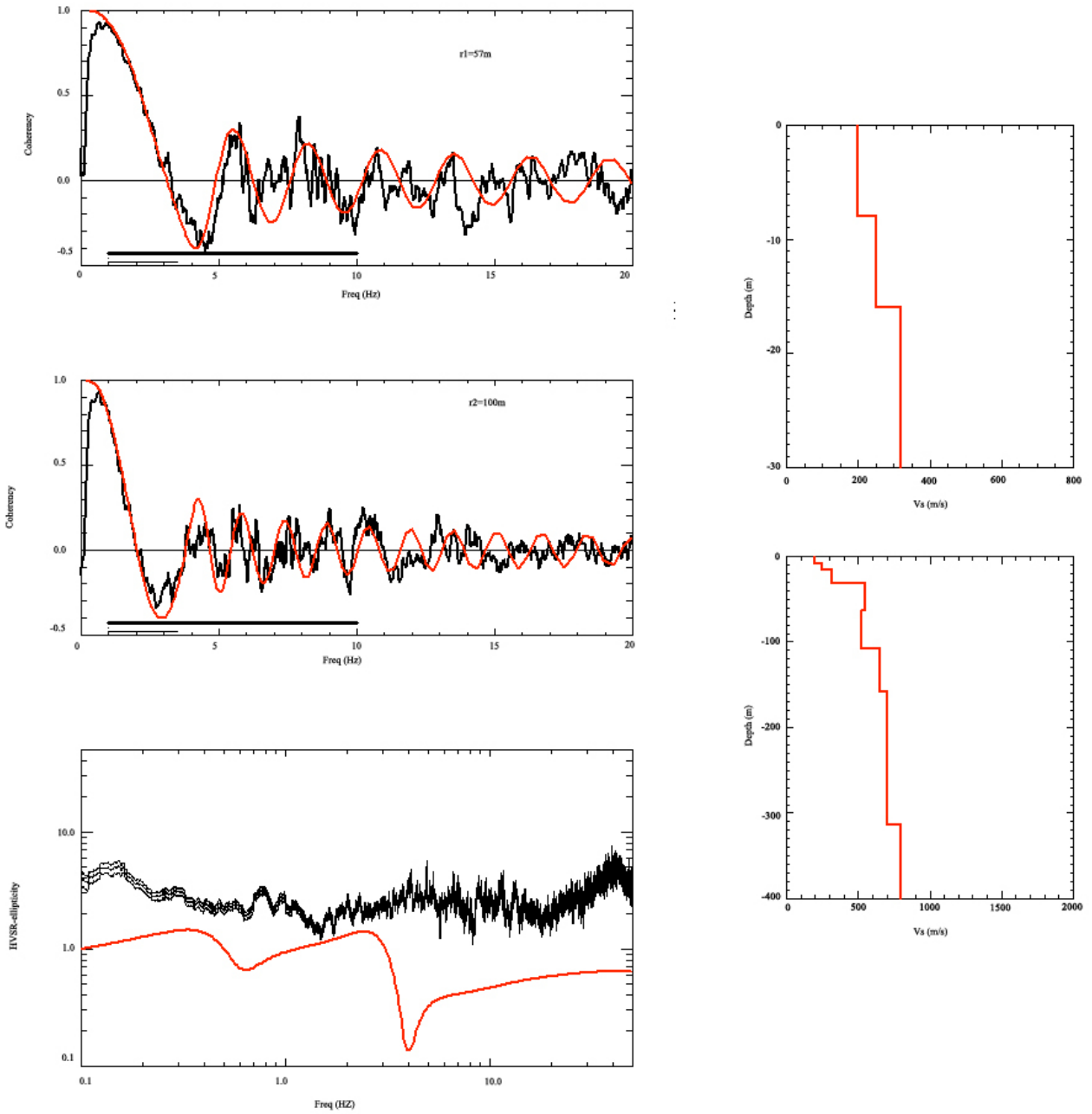

Figure 8. Left column: Coherency curves at Site 4 for station separations of r1 and r2 and HVSR curve. In SPAC curves black is the observed spectra and red is the fitted model SPAC for the Rayleigh fundamental mode. In the HVSR curve, black is the observed spectra and red is the modeled ellipticity curve. Right column: 1D shear wave velocity profiles down to 30 m (top panel) and 400 m depth (bottom panel).

derived a density function for magnitudes corresponding to this model.

Seismic events are random in time; therefore, to estimate the probability of future earthquake events, a stochastic model is required. In classical PSHA, earthquakes are assumed to be independent over time and space, and therefore the Poisson process is the most commonly used model for the temporal occurrence of the earthquakes. According to the Poisson model, the probability that at least one earthquake happens with magnitude greater than the lowest magnitude in the region of interest within a specified time interval t is given by the following expression:

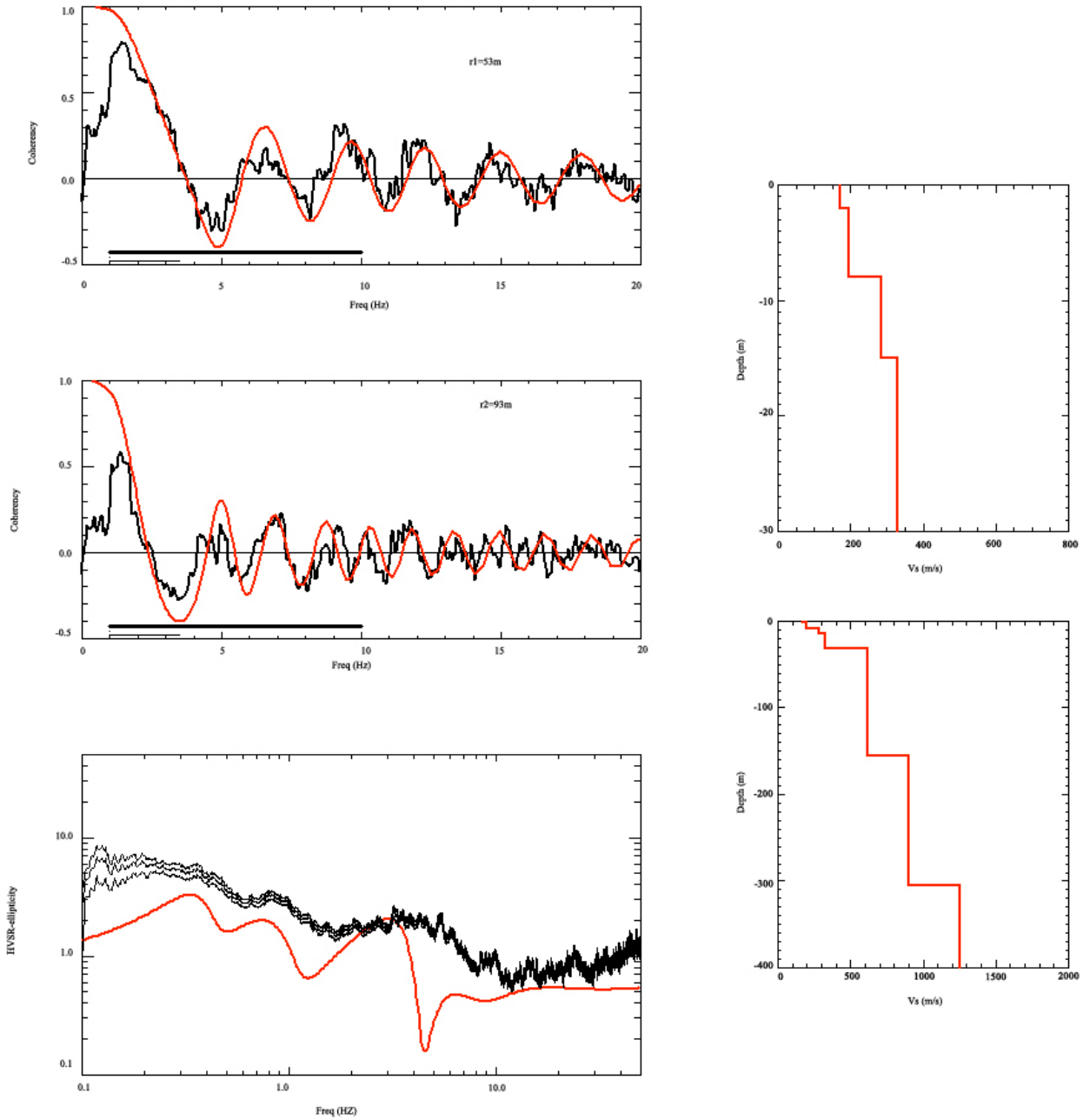

Figure 9. Left column: Coherency curves at Site 5 for station separations of r1 and r2 and HVSR curve. In SPAC curves black is the observed spectra and red is the fitted model SPAC for the Rayleigh fundamental mode. In the HVSR curve, black is the observed spectra and red is the modeled ellipticity curve. Right column: 1D shear wave velocity profiles down to 30 m (top panel) and 400 m depth (bottom panel).

$$\Pr(N \geq 1) = 1 - e^{-vt}, \quad (3)$$

where v is the average number of earthquakes with magnitudes equal to or larger than the lowest magnitude in a given time period (usually 1 year). It is also equal to the reciprocal of the mean interevent time (return period).

The third step of PSHA is to select a ground motion parameter of interest reflecting the seismic hazard, such as peak ground acceleration or spectral acceleration. Additionally, a model that determines the attenuation of this parameter with distance is chosen. Generally, attenuation relationships (or ground motion prediction equations as recently named, GMPEs) are empirical equations that describe amplitudes of ground motion

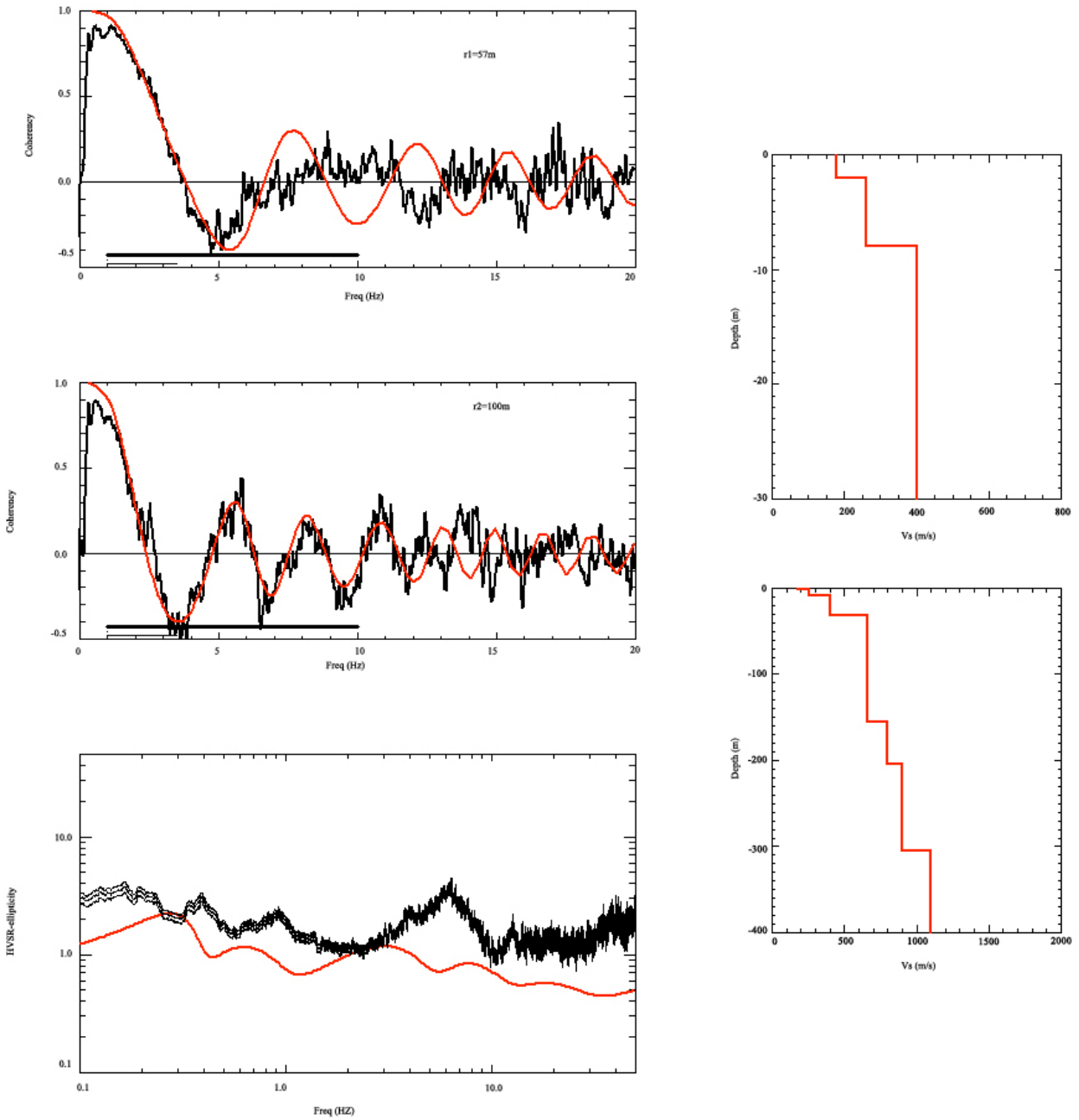

Figure 10. Left column: Coherency curves at Site 6 for station separations of r1 and r2 and HVSR curve. In SPAC curves black is the observed spectra and red is the fitted model SPAC for the Rayleigh fundamental mode. In the HVSR curve, black is the observed spectra and red is the modeled ellipticity curve. Right column: 1D shear wave velocity profiles down to 30 m (top panel) and 400 m depth (bottom panel).

parameters as a function of earthquake magnitude, site-to-source distance, and local soil conditions at the site of interest.

In the last step of PSHA, the probabilities of exceedingly different levels of the selected ground motion parameter are obtained by aggregating the contributions of all seismic sources in the region of interest and its vicinity. A more detailed description can be found in Cornell (1968) and Yucemen (1982).

4.2. Seismic data, source, and ground motion attenuation models

In this study, to conduct seismic hazard analysis of Erzincan, a rectangular domain bounded by 37.5°E to 42.0°E and 38°N to 41°N is considered.

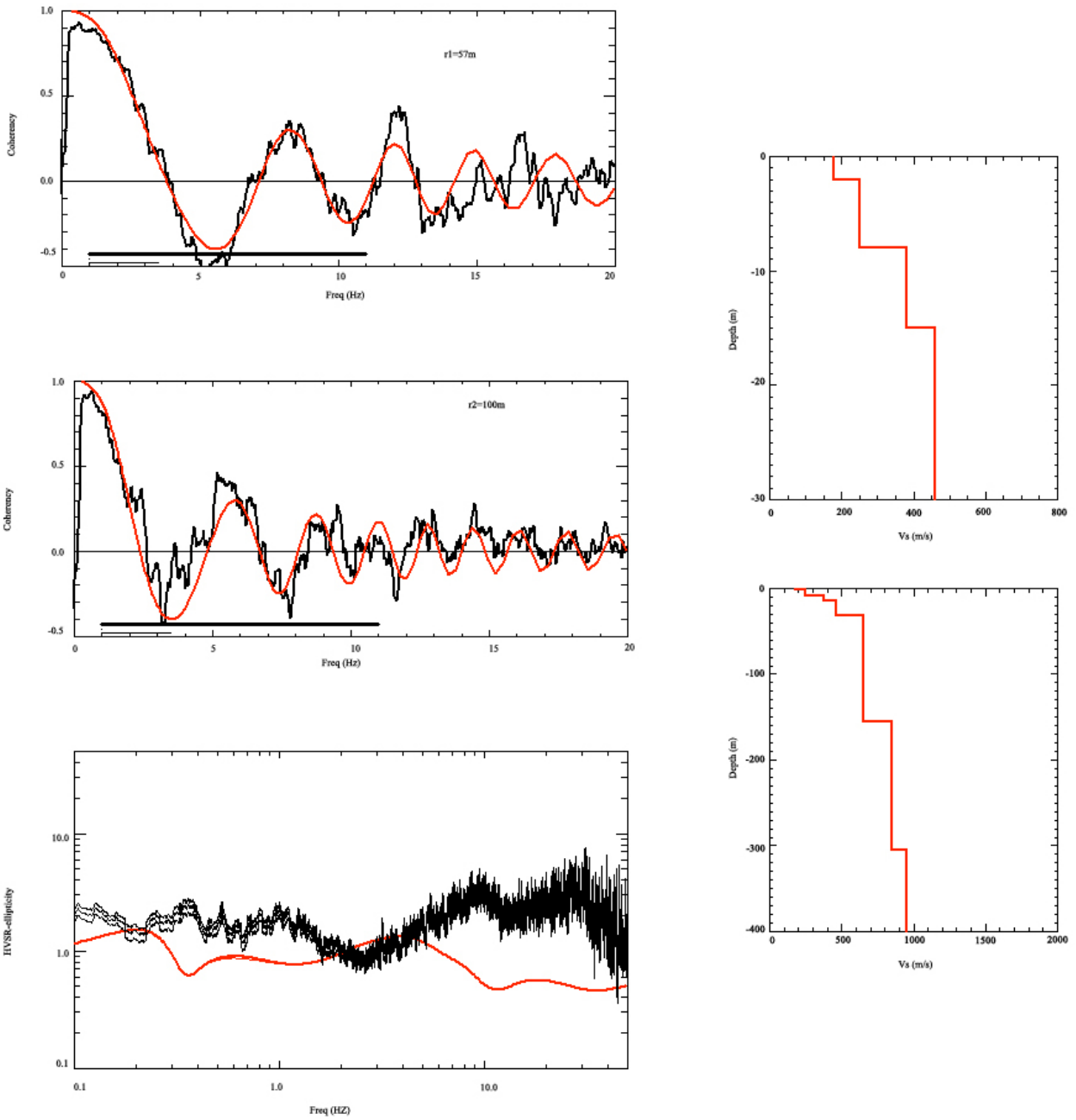

Figure 11. Left column: Coherency curves at Site 7 for station separations of r1 and r2 and HVSR curve. In SPAC curves black is the observed spectra and red is the fitted model SPAC for the Rayleigh fundamental mode. In the HVSR curve, black is the observed spectra and red is the modeled ellipticity curve. Right column: 1D shear wave velocity profiles down to 30 m (top panel) and 400 m depth (bottom panel).

To construct the earthquake catalog, all past earthquakes that occurred between 1900 and 2012 as presented in the seismicity database "from 1900 up to today with M >= 4" as given on the webpage of the Earthquake Department of Disaster and Emergency Management Authority (AFAD; www.deprem.gov.tr) are taken into account. Among different magnitude scales present in the database, the moment magnitude scale (Mw) is selected since it is the most physical descriptor of the seismic energy. Therefore, the other magnitude scales are converted to moment magnitude through the empirical equations developed by Deniz (2006). Figure 15 shows the spatial distribution of all events that occurred within the region of interest. The secondary events (i.e. foreshocks and aftershocks) are

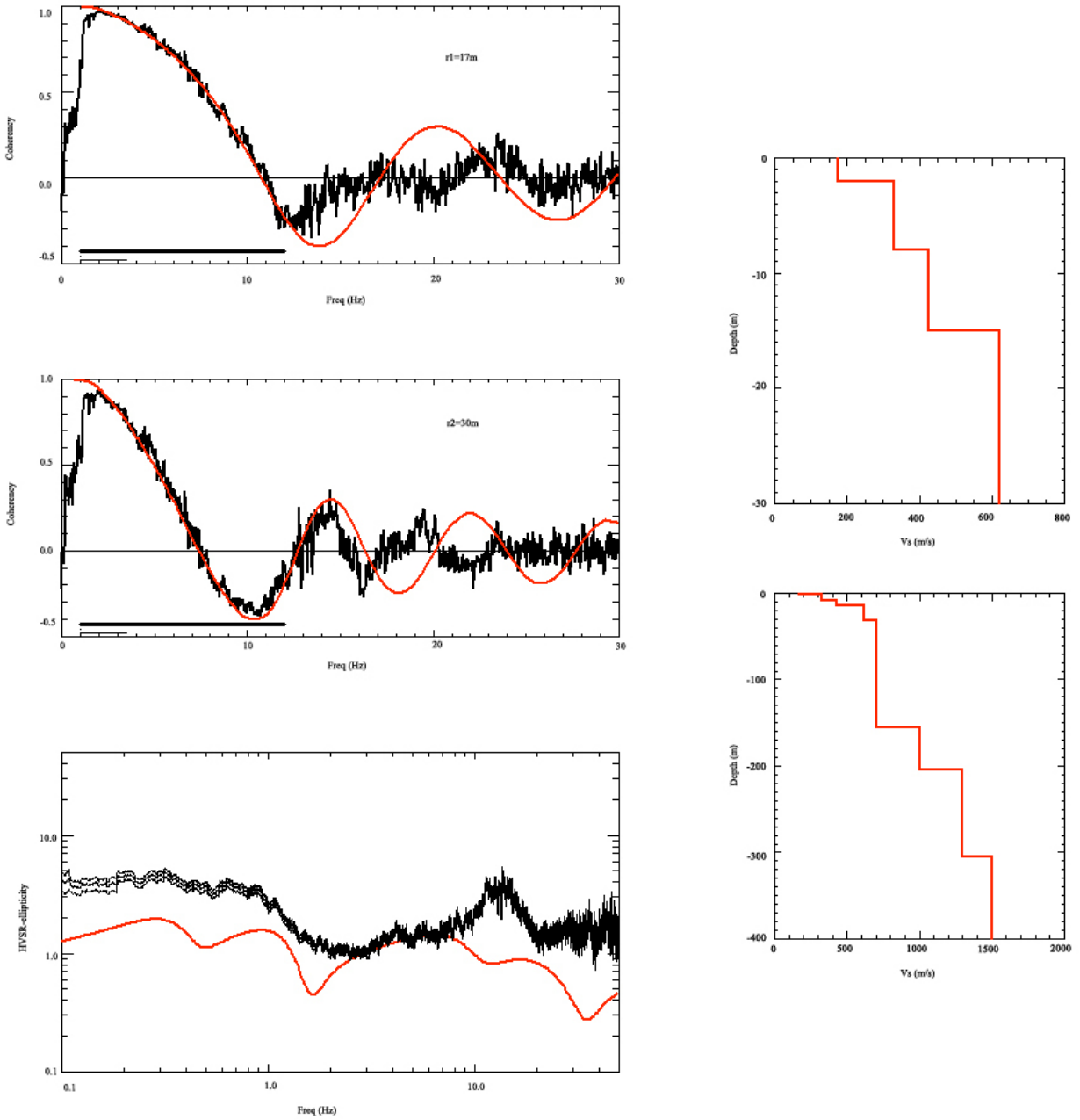

Figure 12. Left column: Coherency curves at Site 8 for station separations of r1 and r2 and HVSR curve. In SPAC curves black is the observed spectra and red is the fitted model SPAC for the Rayleigh fundamental mode. In the HVSR curve, black is the observed spectra and red is the modeled ellipticity curve. Right column: 1D shear wave velocity profiles down to 30 m (top panel) and 400 m depth (bottom panel).

identified by utilizing one simple procedure, based on the assumption that earthquakes that fall into the space and time windows of another earthquake of larger magnitude are identified as secondary events. An alternative database including only main shocks is also constructed by eliminating the secondary events.

In this study, seismic hazard analysis of Erzincan is conducted with two different source models named as Model 1 and Model 2. Only area sources are implemented in Model 1, whereas Model 2 is a hybrid model that considers mostly faults (line sources) with very few area sources in the region of interest. Differences between the results from these two models will be used to study the significance of a hybrid model that employs mostly line sources versus a model with only area sources in hazard analyses.

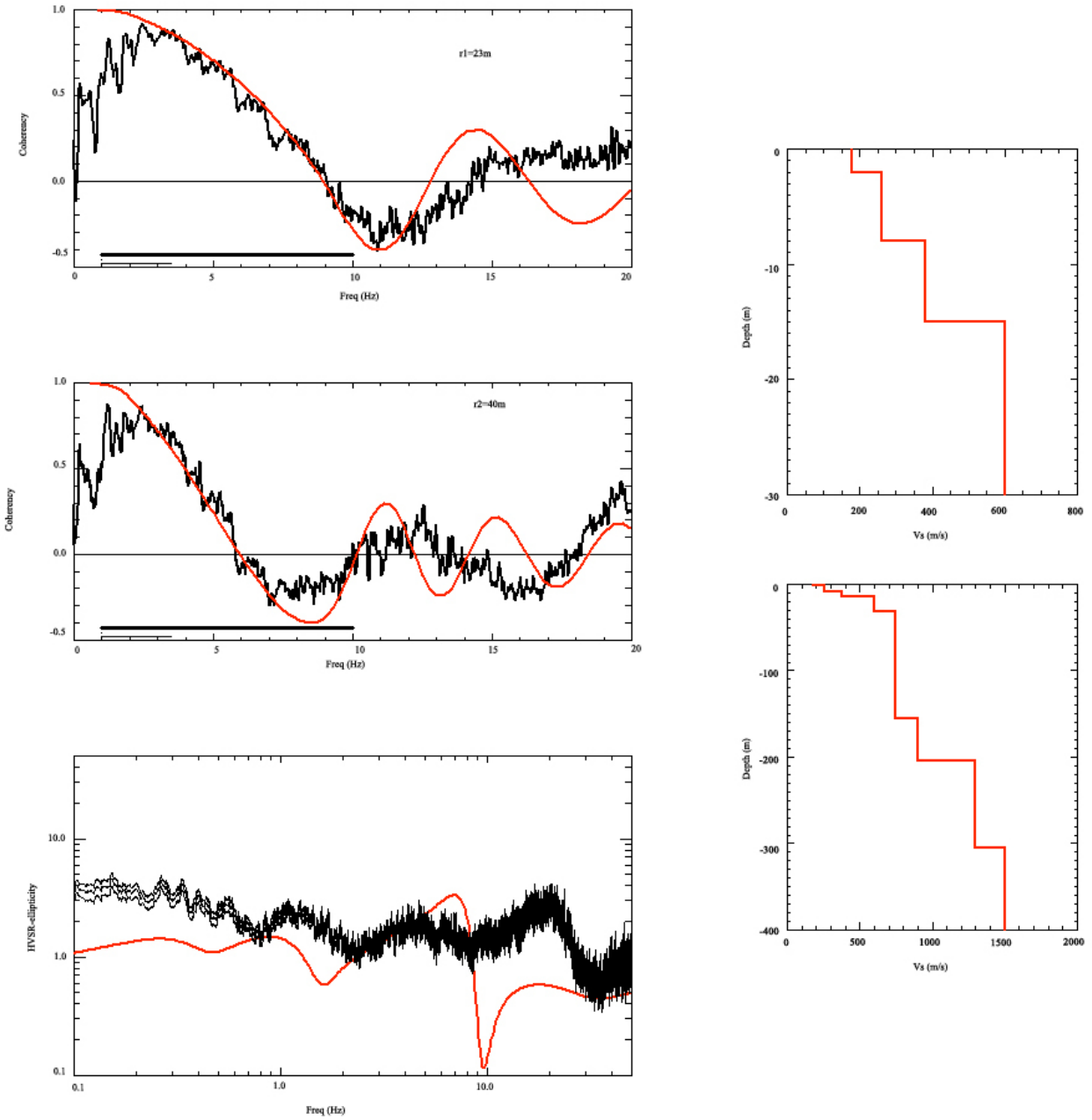

Figure 13. Left column: Coherency curves at Site 9 for station separations of r1 and r2 and HVSR curve. In SPAC curves black is the observed spectra and red is the fitted model SPAC for the Rayleigh fundamental mode. In the HVSR curve, black is the observed spectra and red is the modeled ellipticity curve. Right column: 1D shear wave velocity profiles down to 30 m (top panel) and 400 m depth (bottom panel).

Model 1 uses the seismicity parameters (such as magnitude-recurrence model parameters: α, which is the intercept of the Gutenberg-Richter recurrence relationship, and β, which is the slope of the Gutenberg–Richter recurrence relationship; earthquake activity rates; minimum and maximum magnitude bounds) from Deniz (2006) for the area sources illustrated in Figure 16. The analyses are performed using alternative sets of seismicity parameters presented by Deniz (2006) for both "all events" and "only main shocks" cases considering "catalog completeness" versus "catalog incompleteness" resulting in four different sets (combinations) of parameters. In the statistical estimation of seismicity parameters, Deniz (2006) applied both standard least-squares regression and maximum likelihood methods. It should be noted that exponential magnitude distribution is utilized for all area sources in this model.

Table 1. Vs30 values obtained via MMSPAC analyses at the sites of interest.

Site	1	2	3	4	5	6	7	8	9
Vs30 (m/s)	256	569	304	287	267	336	348	427	387

In Model 2, which is a hybrid model, the majority of the area sources of Model 1 are replaced with active faults (line sources). All of the line sources as well as the corresponding seismicity parameters are determined particularly in this paper. To determine these faults, the fault map prepared by the General Directorate of Mineral Research and Exploration (MTA) in 2012 is considered. However, for those seismic activities that belong to none of the specified line sources, very few area sources are assumed. Figure 17 represents the entire 58 line sources

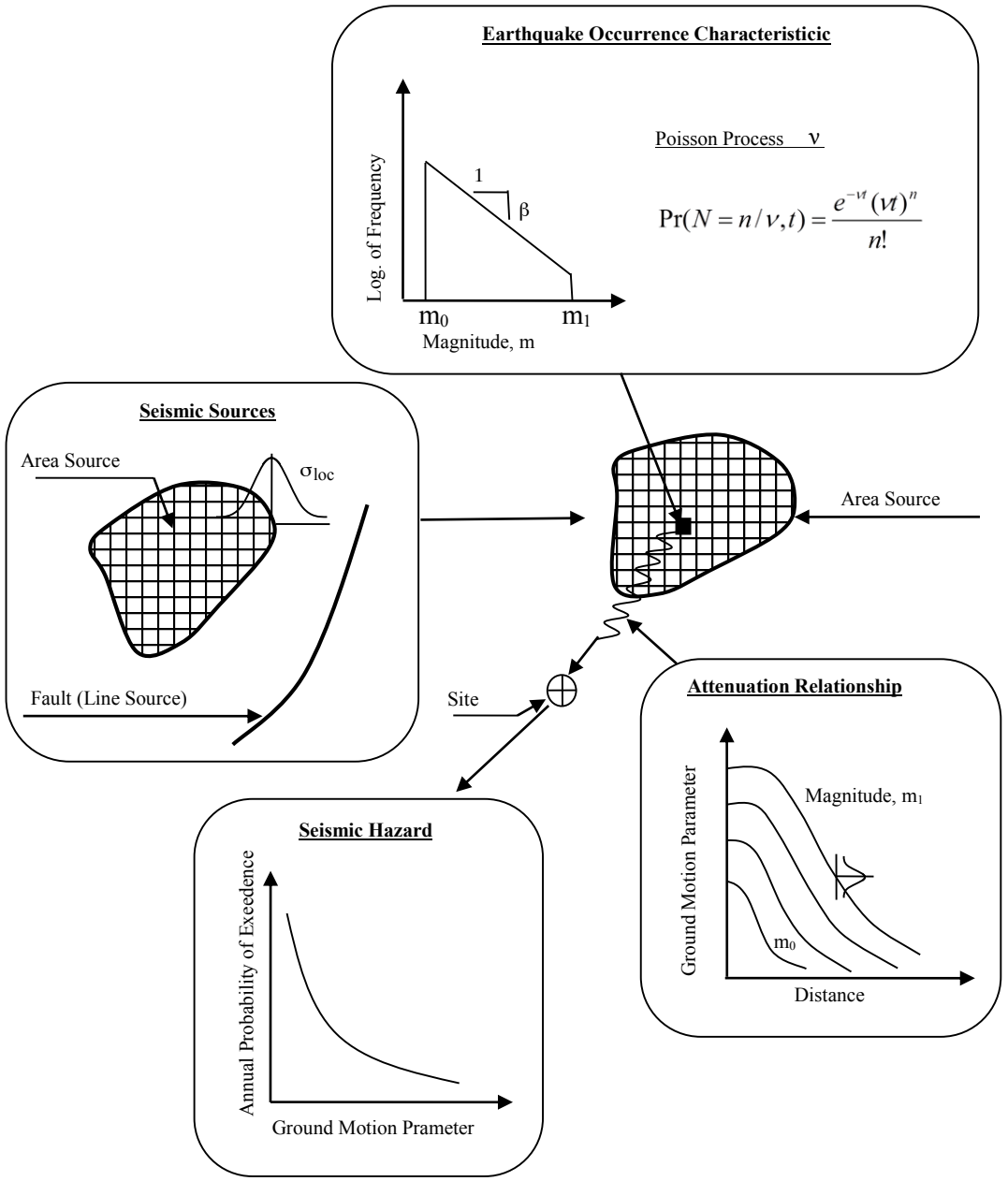

Figure 14. Main steps of probabilistic seismic hazard analysis.

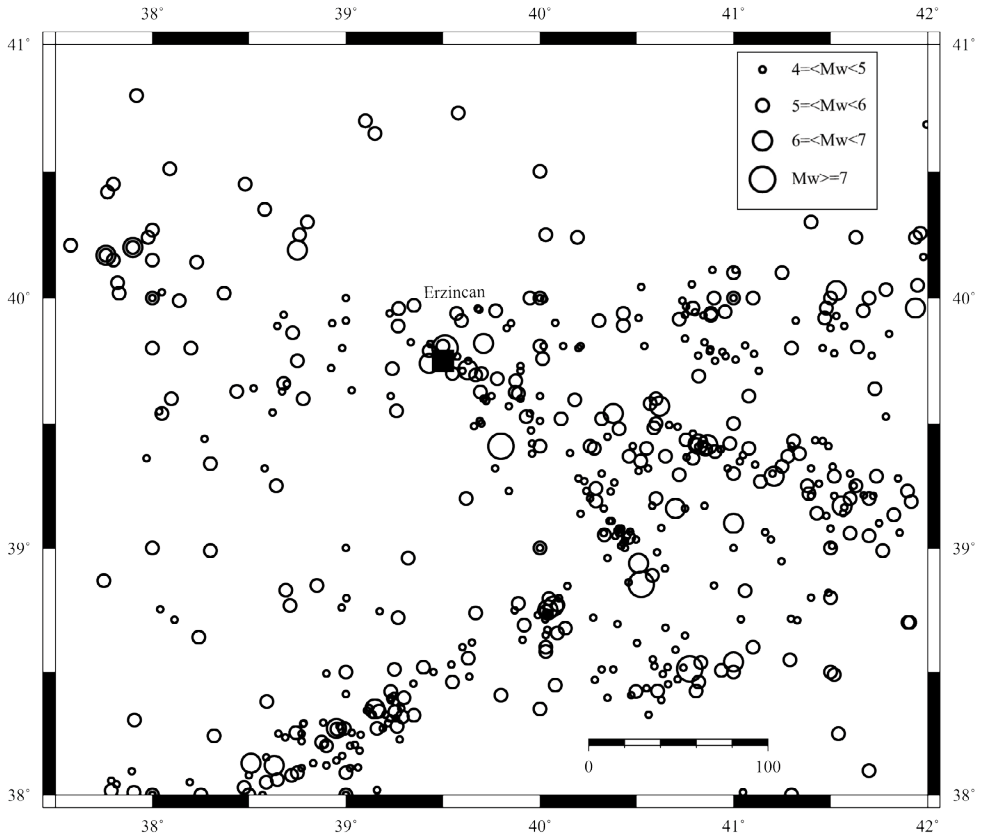

Figure 15. Spatial distribution of all earthquakes around Erzincan city center.

as well as the 2 area sources considered in Model 2. The maximum magnitude of each line source is assigned by considering the past events and moment magnitude calculated by the following Wells and Coppersmith (1994) equation:

$$M_w = 5.08 + 1.16 \times \log(SRL), \quad (4)$$

where *SRL* is defined as the surface rupture length in km. Table 2 lists the source mechanisms as well as the maximum magnitudes estimated for each seismic source in Model 2. Four different sets of seismicity parameters are determined for each seismic source by considering the aforementioned two seismicity catalogs as well as the incompleteness of them in terms of smaller magnitude earthquakes. In Model 2, the characteristic earthquake model is assumed for all line sources while maximum magnitude obtained from the regional catalog is assumed for area sources.

In this study, to express the attenuation of ground motion with distance, magnitude, and soil conditions, two alternative GMPEs are used with equal weights of 0.5 in the logic tree. One of them is the ground motion attenuation relationship developed by Kalkan and Gülkan (2004) based on a Turkish database. This model predicts peak ground acceleration (PGA) and response spectral ordinates at 5% critical damping in the range of 0.1 to 2.0 s over the full range of magnitudes (Mw = 4 to 7.5) and for Joyner–Boore distances of up to 250 km. In that study, a total of 112 strong ground motion records from 57 earthquakes that occurred between 1976 and 2003 were employed. The second GMPE was developed by Boore and Atkinson (2008) within the Next Generation of Ground Motion Attenuation Models project (Power et al., 2008). This equation is developed using an extensive database of thousands of records, compiled from shallow crustal earthquakes in active tectonic regions all over the world including earthquakes from California and Turkey.

For both models, one of the most significant parameters that affect the ground motion amplitudes considerably is Vs30. Thus, it is important to use precise Vs30 values to accurately represent the local site conditions. In this study, for all 9 sites of interest, Vs30 values as determined and presented in Section 3 are employed.

4.3. Results of PSHA

The results of PSHA at 9 sites are expressed in terms of annual exceedance rates for different levels of selected peak ground motion parameters such as PGA, spectral

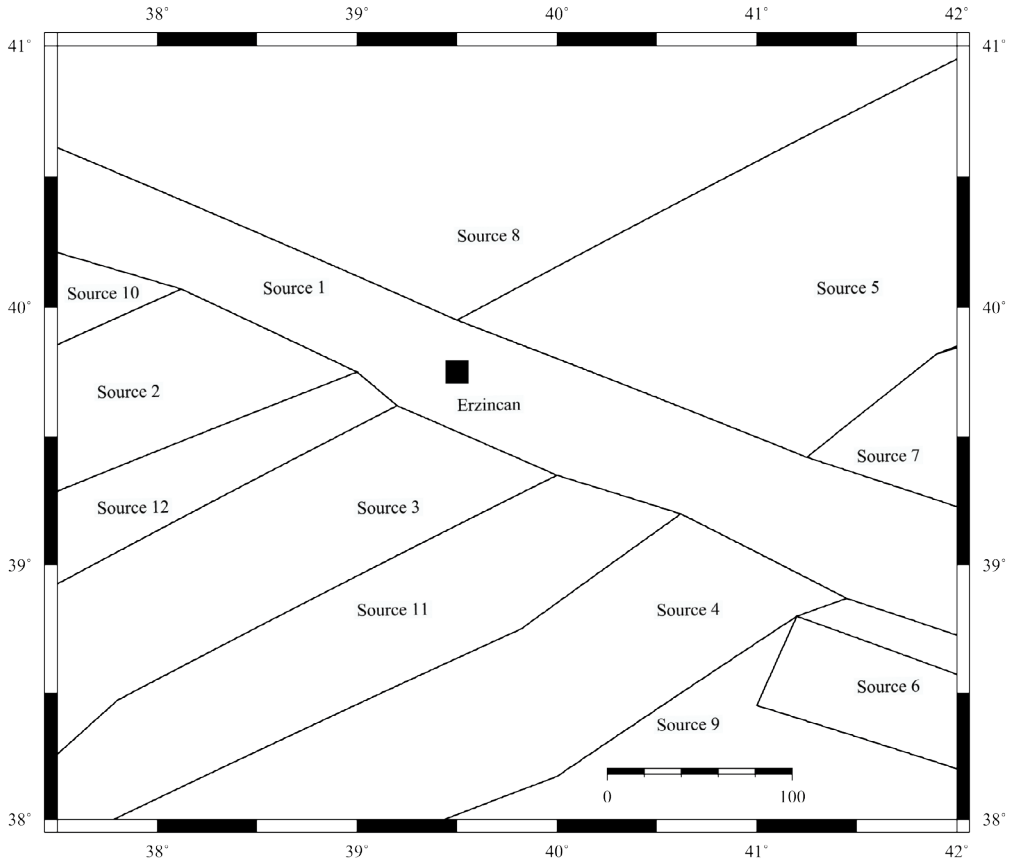

Figure 16. Earthquake sources considered in Model 1.

acceleration (SA) at T = 0.2 s, and SA at T = 1 s. The SA values presented are spectral accelerations with 5% damping computed directly from the numerical solution of the dynamic equation of motion involving the simulated acceleration time series. In addition, hazard curves of all 9 selected sites are presented in Figures 18–26 and the results for all 9 sites are summarized in Tables 3–5 for selected return periods of 475, 975, and 2475 years. In these tables, results for Model 1, Model 2, and the weighted average of these two models based on logic tree method are presented.

Figures 18–26 and Tables 3–5 show that sites on the softer soils (e.g., Site 1) experience higher ground motion amplitudes for both Model 1 and 2, while the sites on the stiffer soils (e.g., Site 2) are subjected to lower amplitudes. This observation is true for PGA as well as spectral accelerations regardless of the source model used in the analyses. The effect of soil conditions on hazard results is similar regardless of return periods. These differences in ground motion amplitudes show that site conditions affect the hazard results considerably. Weighted average results corresponding to the 475-year return period suggest that for most sites PGA values exceed the corresponding PGA of the design spectra (0.4 *g*) as defined in the current Turkish Seismic Code (Turkish Ministry of Public Works and Settlement, 2007) for seismic zone 1, which also corresponds to the 475-year return period. This is an important finding considering the vulnerability of the existing nonengineered buildings in the region that do not even comply with the code requirements.

Finally, a comparison between Model 1 and Model 2 reveals that the results from Model 1 are almost half those from Model 2. This observation suggests that use of area sources (as in Model 1) in regions of nearby active faults could yield lower hazard values than the line sources. This is mainly because the activity rates are distributed over areas in area source models instead of those along fault lines in line source models (Yılmaz-Öztürk, 2008; Yılmaz and Yücemen, 2015). However, there can be exceptions to this observation in regions of low activity (unlike Erzincan) where seismicity is modeled with area sources rather than line sources, which may cause an increase in seismic hazard values at the regions near the boundaries of area sources.

5. Deterministic seismic hazard analyses

In some cases, hazard analyses are required to assess the seismic hazard of a region under specific earthquake

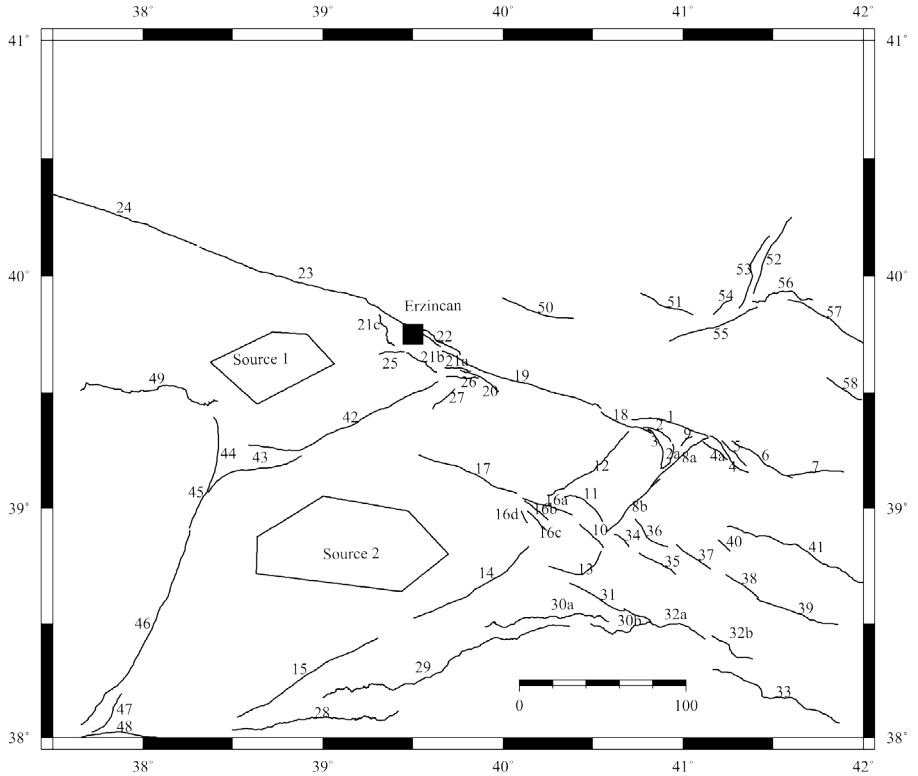

Figure 17. Earthquake sources considered in Model 2.

scenarios. This procedure is called deterministic seismic hazard analysis (DSHA). Generally, these analyses involve use of empirical ground motion prediction equations given a particular Mw, source-to-site distance, and site conditions. Recently, ground motion simulations using complex models of wave propagation are also employed for deterministic hazard analyses. In this study, the latter approach is employed to evaluate the ground motion distribution for possible future earthquakes in Erzincan. Ground motion simulations are preferred herein since they provide the full time series of acceleration, instead of GMPEs that provide only the peak or spectral ground motion parameters.

The stochastic finite-fault method is employed in this study to simulate the ground motion of the selected set of scenario earthquakes in Erzincan.

5.1. Methodology for DSHA

Strong ground motion simulation methods are employed to estimate reliable synthetic records by modeling the earthquake source mechanisms and regional wave propagation. In this study, stochastic finite fault modeling as introduced by Motazedian and Atkinson (2005) is employed. This method was used previously to effectively model earthquakes all over the world as well as recent Turkish events (e.g., Motazedian and Moinfar, 2006; Castro et al., 2008; Ugurhan and Askan, 2010; Ugurhan et al., 2012).

The stochastic finite-fault method simulates ground motions that radiate from a rectangular finite-fault divided into subfaults, each of which is modeled as a stochastic point source with an w^{-2} spectrum. In this model, the hypocenter of the earthquake is assumed to be on one of the subfaults, and the rupture propagates radially from the hypocenter. Each subfault is triggered when the rupture reaches the center of that subfault. The contribution of all subfaults is summed with appropriate time delays in order to obtain the entire contribution of the fault plane to the seismic field, at any observation point:

$$A(t) = \sum_{i=1}^{nl} \sum_{j=1}^{nw} A_{ij}\left(t + \Delta t_{ij}\right), \quad (5)$$

where $A(t)$ is the acceleration obtained from the entire fault; A_{ij} is the contribution of the ij^{th} subfault to the amplitude; nl and nw and are the number of subfaults along the length and width of the fault, respectively. The time delay for each element, Δt_{ij}, is the summation of the time required for the rupture front to reach the element and the time required for the shear-wave to reach the receiver after the element has been triggered (Beresnev and Atkinson, 1997).

In the dynamic corner frequency approach, the total

Table 2. Seismic source zones of Model 2 and the corresponding expected maximum magnitude (m_1) values.

Seismic source no.	Fault type	m_1
1	Right-lateral strike-slip	6.9
2	Normal	6.5
2a	Normal	6.4
3	Normal	6.6
4	Right-lateral strike-slip	6.7
4a	Right-lateral strike-slip	6.5
5	Right-lateral strike-slip	a6.2
6	Right-lateral strike-slip	6.8
7	Right-lateral strike-slip	6.8
8a	Left-lateral strike-slip	7.2
8b	Left-lateral strike-slip	6.8
9	Normal	6.1
10	Right-lateral strike-slip	6.5
11	Right-lateral strike-slip	6.7
12	Left-lateral strike-slip	7.1
13	Normal	6.8
14	Left-lateral strike-slip	7.1
15	Left-lateral strike-slip	7.3
16a	Right-lateral strike-slip	6.7
16b	Right-lateral strike-slip	6.4
16c	Right-lateral strike-slip	6.4
16d	Right-lateral strike-slip	6
17	Right-lateral strike-slip	7.1
18	Right-lateral strike-slip	6.7
19	Right-lateral strike-slip	7.3
20	Right-lateral strike-slip	6.6
21a	Normal	6.4
21b	Normal	6.5
21c	Normal	6.6
22	Normal	6.8
23	Right-lateral strike-slip	7.9
24	Right-lateral strike-slip	7.9
25	Right-lateral strike-slip	6.4
26	Left-lateral strike-slip	6.5
27	Left-lateral strike-slip	6.4
28	Reverse	7.3
29	Reverse	7.6
30a	Reverse	7.2
30b	Reverse	6.8
31	Right-lateral strike-slip	6.8
32a	Reverse	7
32b	Reverse	6.7
33	Reverse	7.2
34	Normal	6.2
35	Right-lateral strike-slip	6.6
36	Right-lateral strike-slip	6.6
37	Right-lateral strike-slip	6.6
38	Right-lateral strike-slip	6.6
39	Right-lateral strike-slip	7
40	Right-lateral strike-slip	6.1
41	Reverse	7.3
42	Left-lateral strike-slip	7.4
43	Left-lateral strike-slip	7.1
44	Left-lateral strike-slip	6.9
45	Left-lateral strike-slip	6.6
46	Left-lateral strike-slip	7.5
47	Left-lateral strike-slip	6.7
48	Left-lateral strike-slip	6.9
49	Reverse	7.3
50	Right-lateral strike-slip	6.9
51	Right-lateral strike-slip	6.8
52	Right-lateral strike-slip	7
53	Right-lateral strike-slip	6.9
54	-	6.3
55	Left-lateral strike-slip	7
56	Reverse	6.8
57	Right-lateral strike-slip	7
58	Right-lateral strike-slip	6.6
Source 1	Area source	5.8
Source 2	Area source	5.5

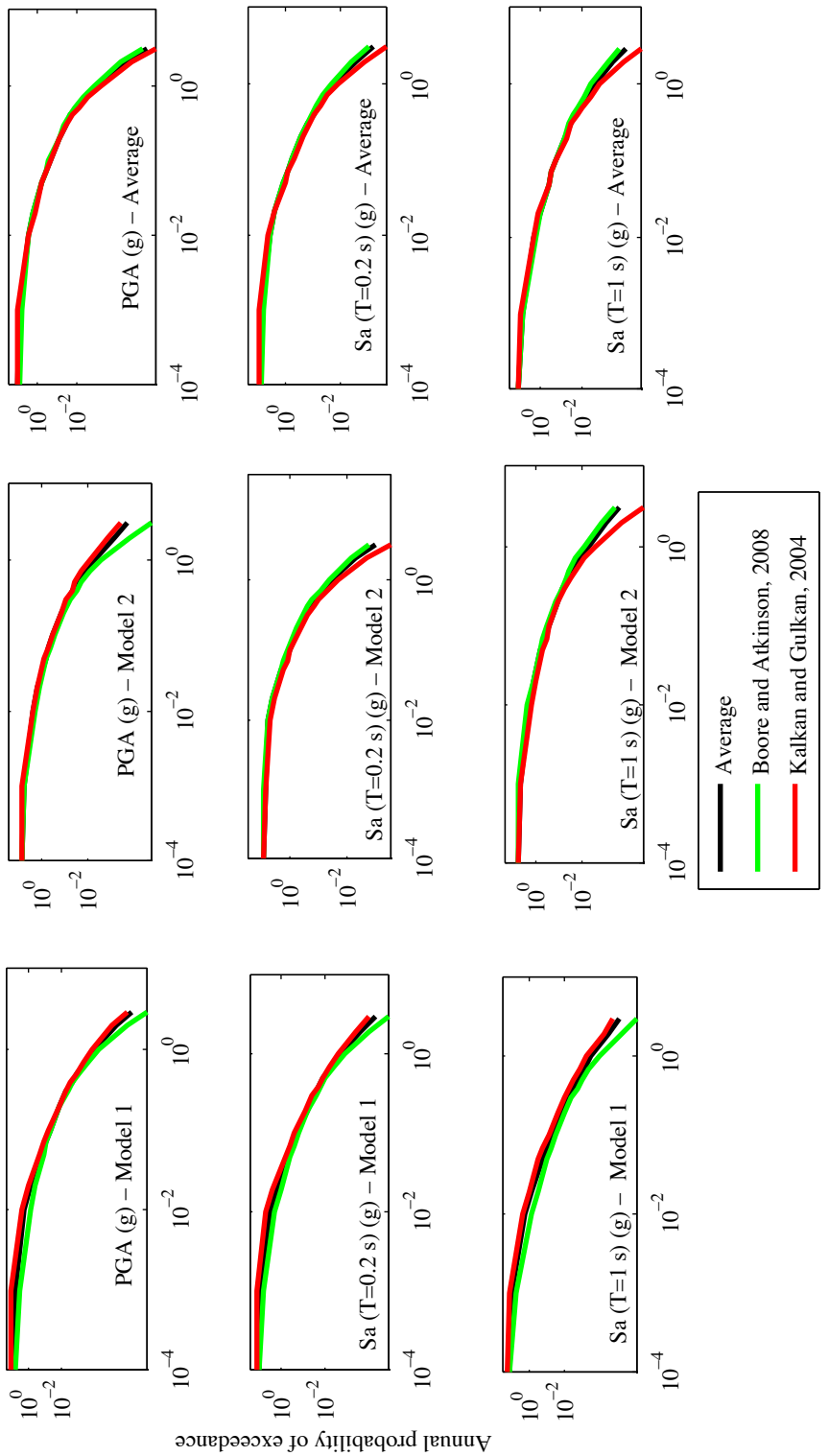

Figure 18. Seismic hazard curves of Site 1 for different GMPEs.

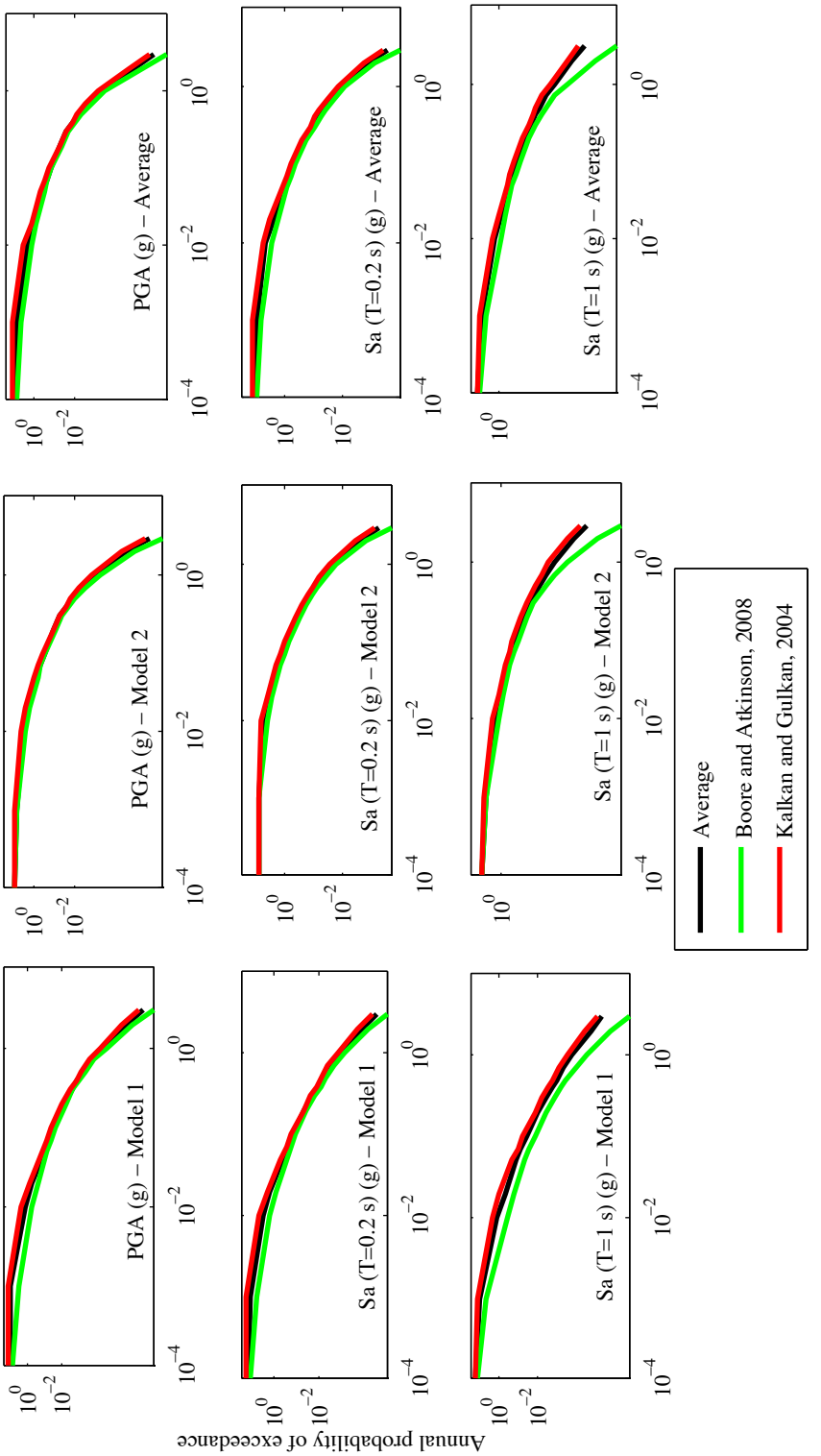

Figure 19. Seismic hazard curves of Site 2 for different GMPEs.

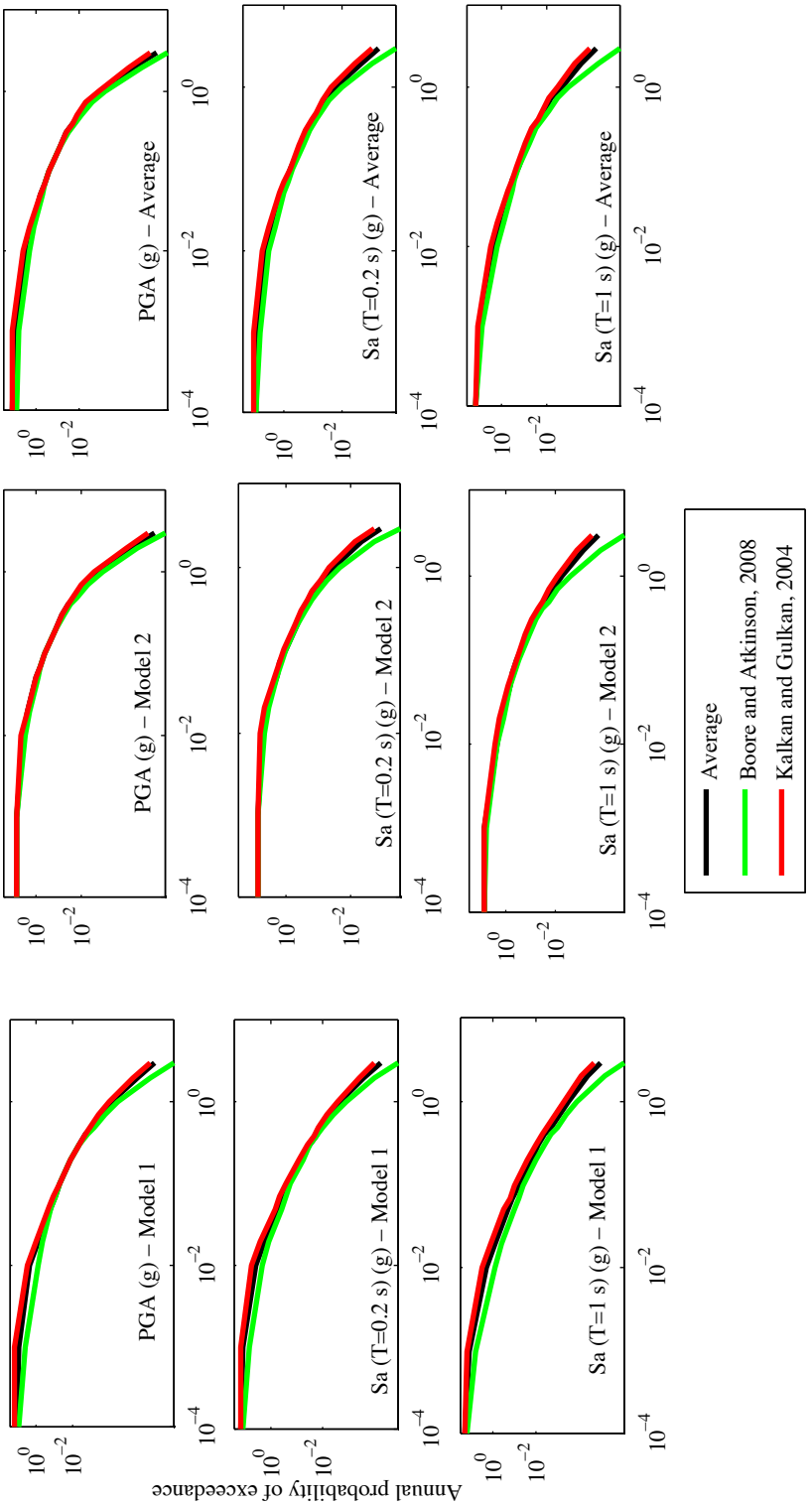

Figure 20. Seismic hazard curves of Site 3 for different GMPEs.

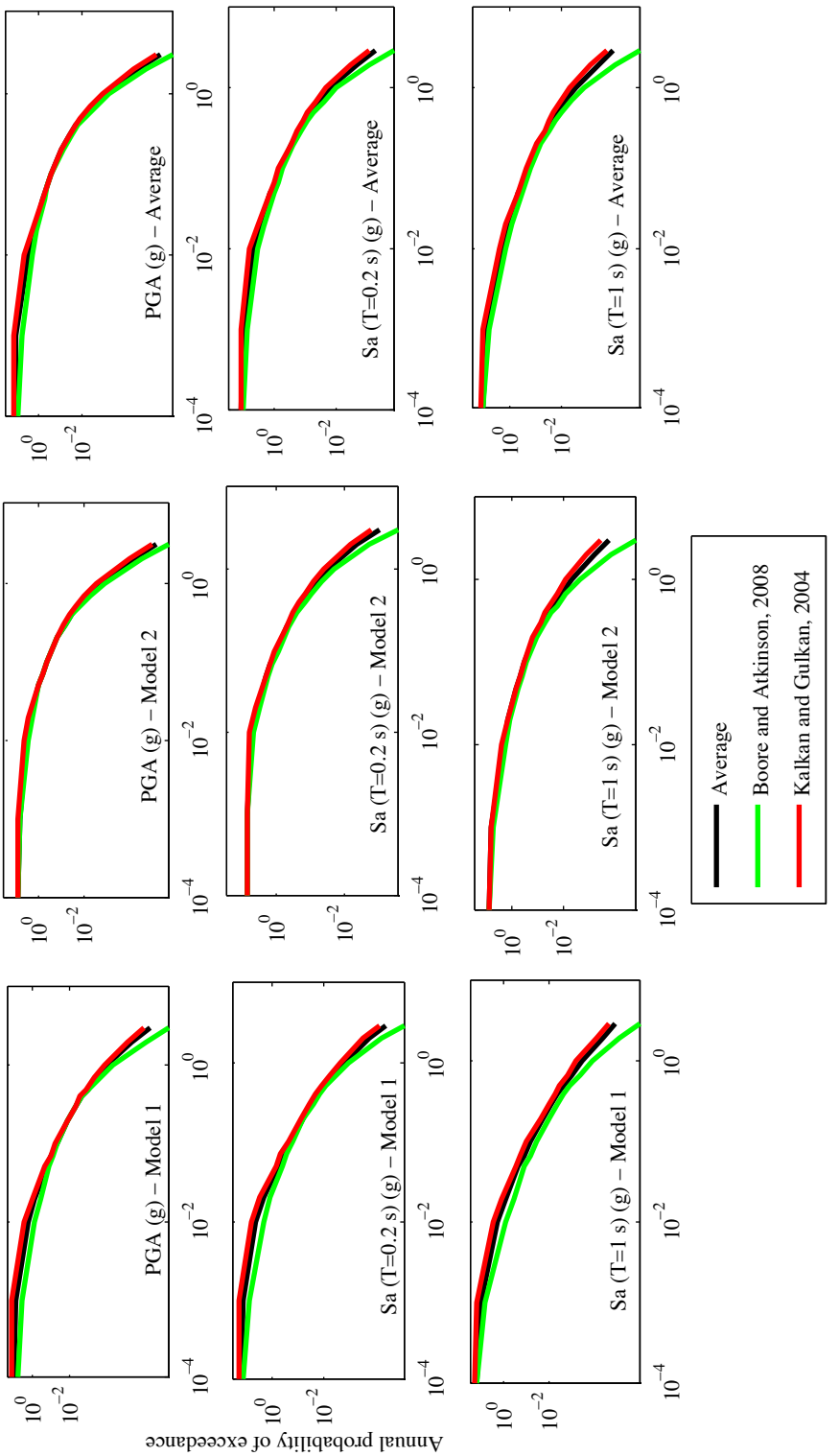

Figure 21. Seismic hazard curves of Site 4 for different GMPEs.

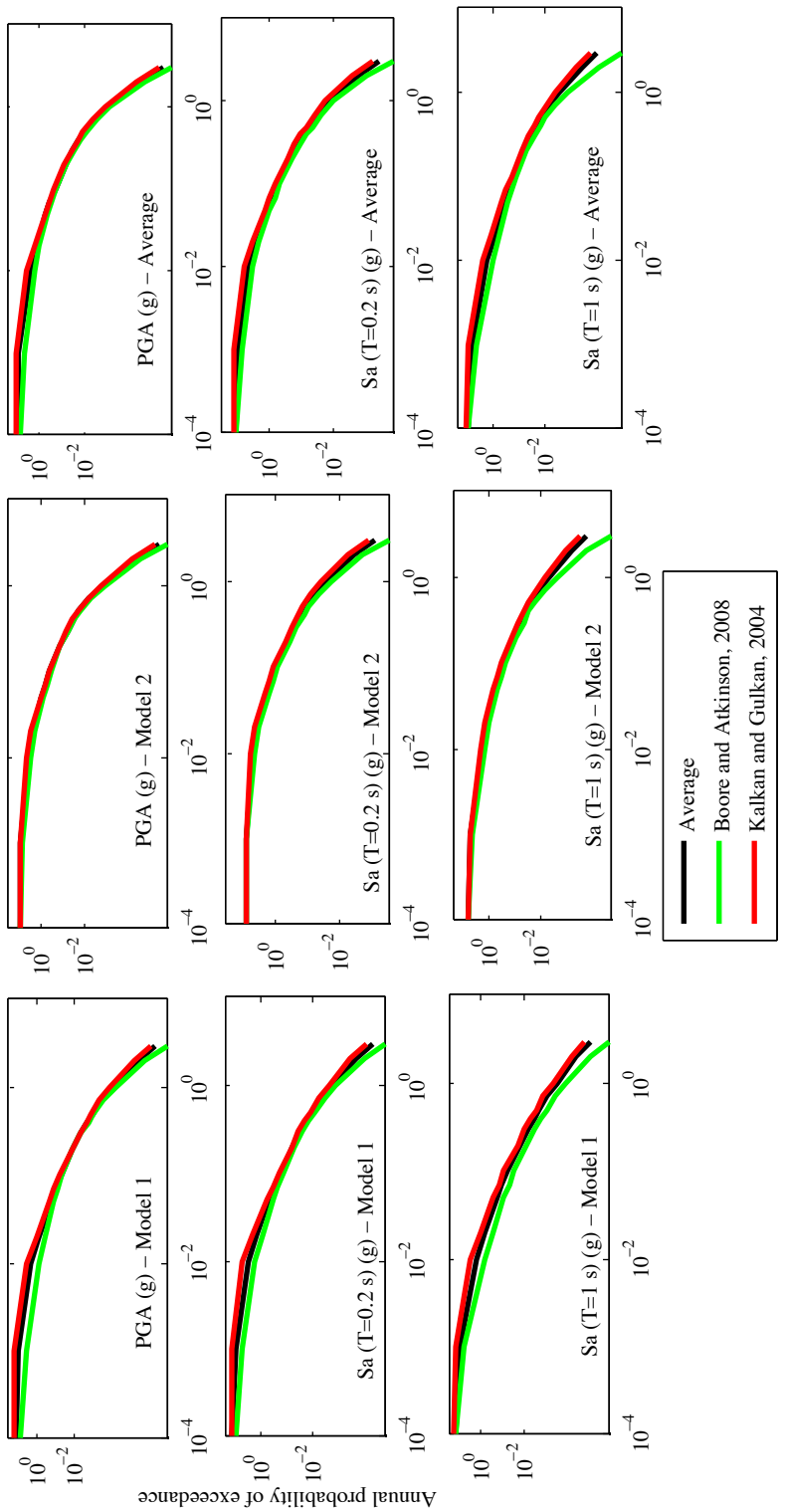

Figure 22. Seismic hazard curves of Site 5 for different GMPEs.

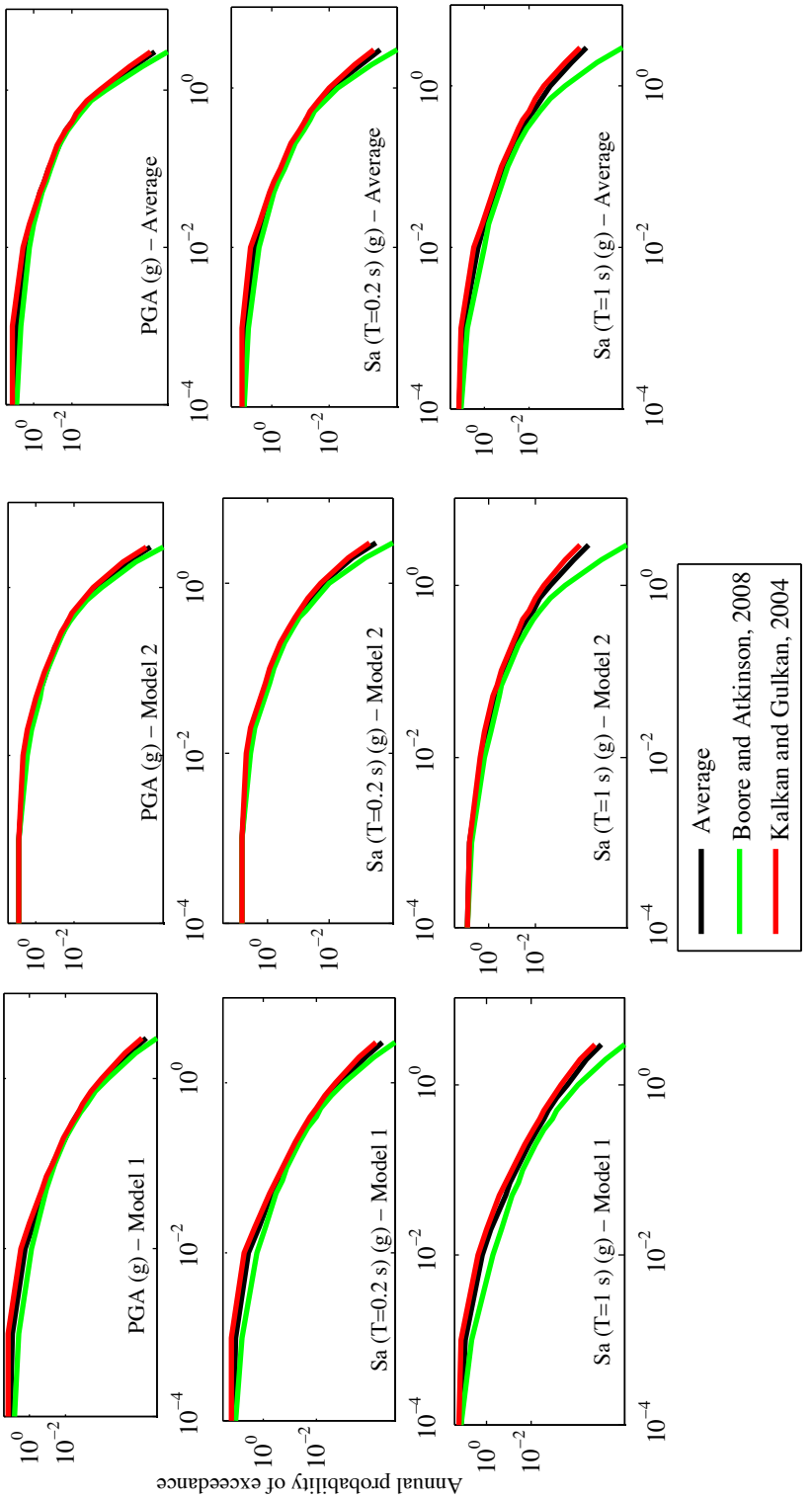

Figure 23. Seismic hazard curves of Site 6 for different GMPEs.

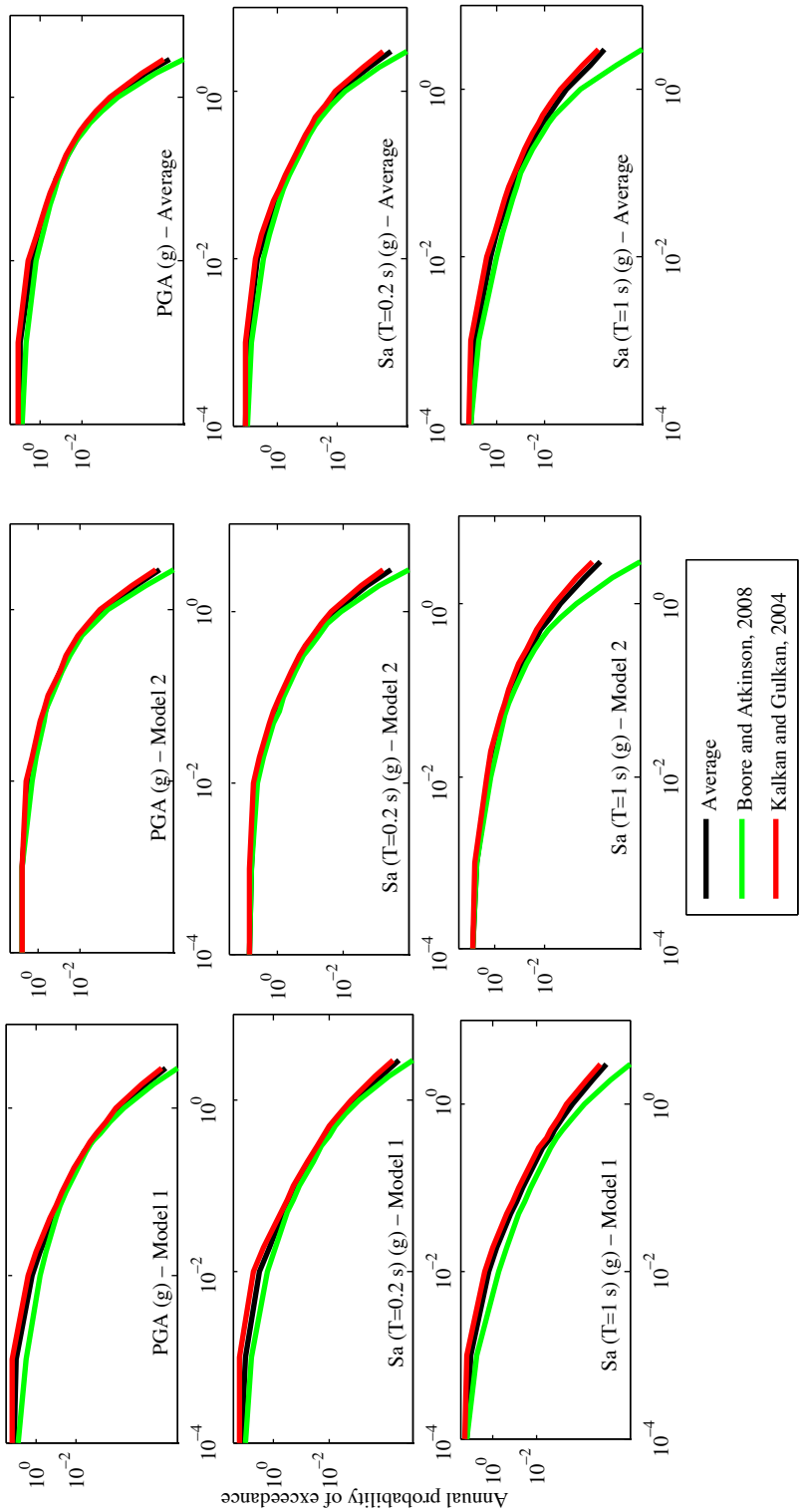

Figure 24. Seismic hazard curves of Site 7 for different GMPEs.

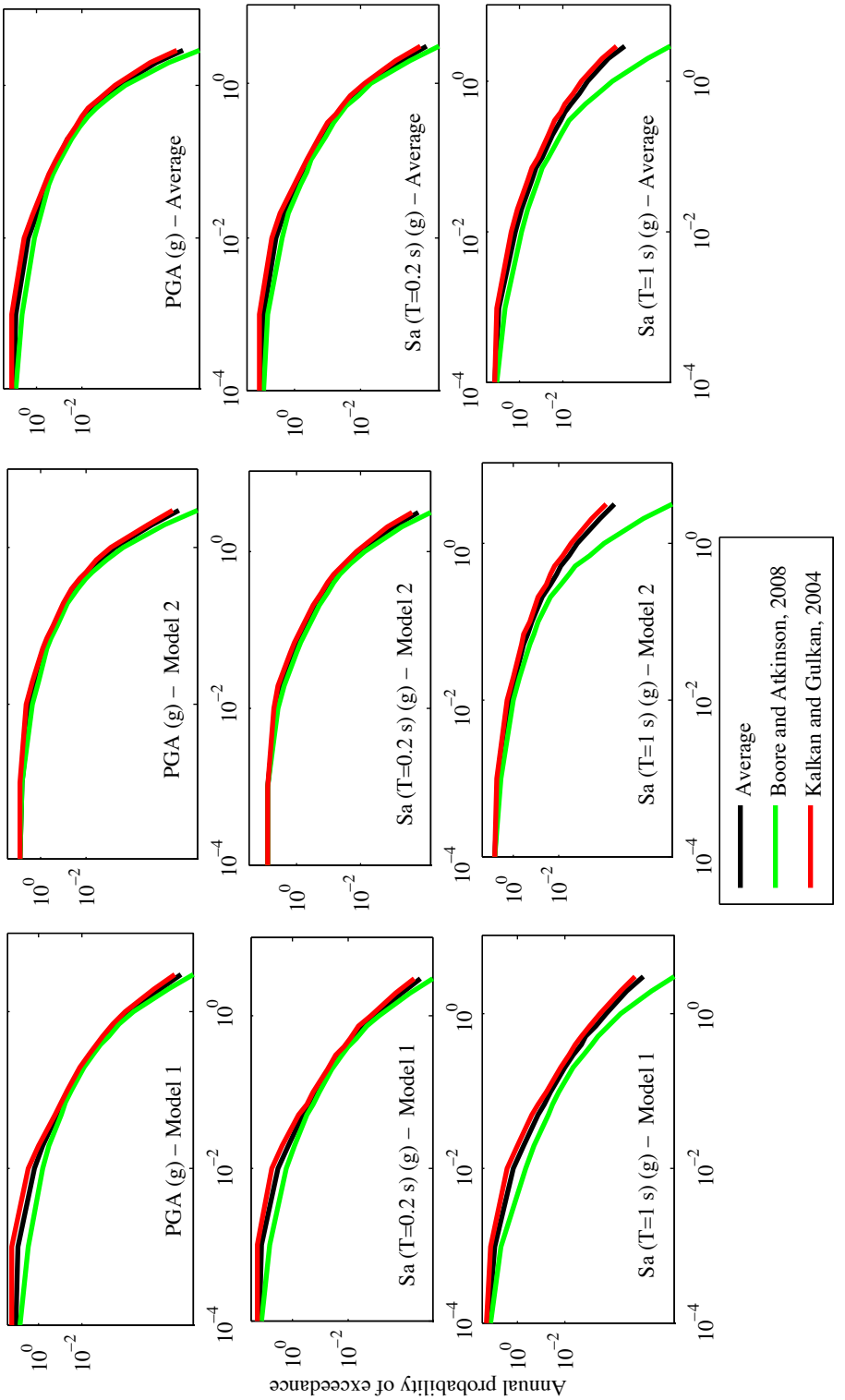

Figure 25. Seismic hazard curves of Site 8 for different GMPEs.

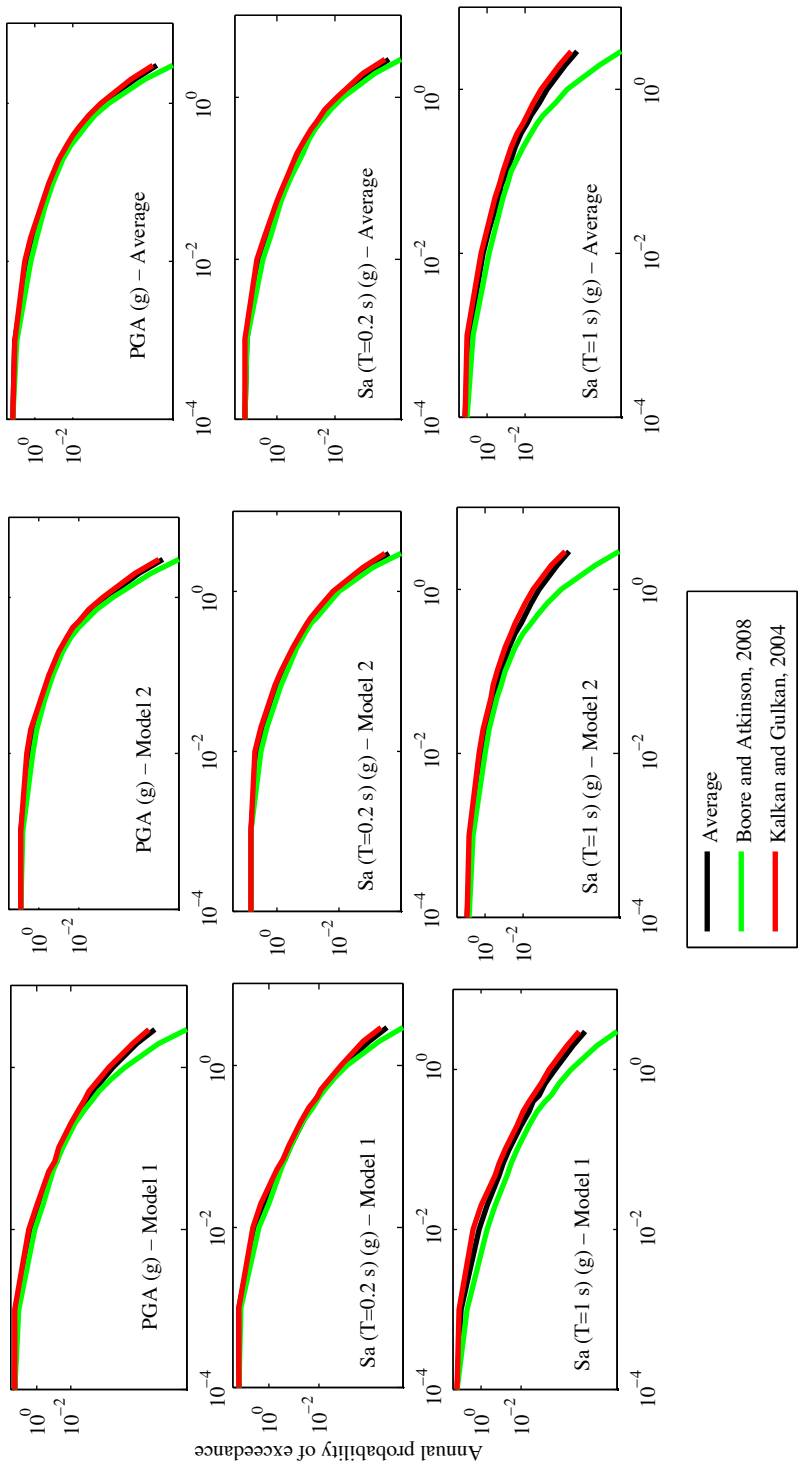

Figure 26. Seismic hazard curves of Site 9 for different GMPEs.

Table 3. Results of PSHA in terms of PGA for the different return periods and models considered.

Site no.	PGA (*g*)								
	Return period : 475 years			Return period : 1000 years			Return period : 2475 years		
	Model 1	Model 2	Average	Model 1	Model 2	Average	Model 1	Model 2	Average
Site 1	0.40	0.96	0.87	0.51	1.14	0.99	0.66	1.37	1.60
Site 2	0.34	0.85	0.74	0.44	1.02	0.92	0.58	1.21	1.30
Site 3	0.40	0.98	0.88	0.51	1.15	1.00	0.66	1.39	1.62
Site 4	0.40	0.98	0.88	0.51	1.15	1.00	0.66	1.39	1.62
Site 5	0.39	0.95	0.86	0.50	1.13	0.99	0.65	1.36	1.58
Site 6	0.37	0.73	0.66	0.47	0.87	0.81	0.62	1.06	0.98
Site 7	0.37	0.75	0.67	0.48	0.90	0.83	0.62	1.09	0.99
Site 8	0.35	0.70	0.63	0.45	0.83	0.75	0.59	1.02	0.95
Site 9	0.33	0.72	0.64	0.42	0.85	0.77	0.55	1.05	0.96

Table 4. Results of PSHA in terms of SA (T = 0.2 s) for the different return periods and models considered.

Site no.	Spectral acceleration (T = 0.2 s) (*g*)								
	Return period : 475 years			Return period : 1000 years			Return period : 2475 years		
	Model 1	Model 2	Average	Model 1	Model 2	Average	Model 1	Model 2	Average
Site 1	0.95	2.43	2.08	1.21	2.98	2.70	1.62	3.83	3.06
Site 2	0.80	2.08	1.91	1.04	2.51	2.25	1.38	3.15	2.86
Site 3	0.96	2.45	2.10	1.23	3.01	2.72	1.64	3.86	3.07
Site 4	0.97	2.45	2.11	1.23	3.01	2.72	1.64	3.87	3.07
Site 5	0.92	2.34	1.99	1.18	2.86	2.62	1.57	3.65	3.02
Site 6	0.86	1.81	1.82	1.12	2.21	1.97	1.48	2.75	2.64
Site 7	0.87	1.87	1.85	1.12	2.27	1.99	1.49	2.83	2.69
Site 8	0.81	1.65	1.74	1.05	2.04	1.93	1.40	2.51	2.41
Site 9	0.81	1.70	1.77	1.05	2.08	1.94	1.37	2.59	2.48

Table 5. Results of PSHA in terms of SA (T = 1 s) for the different return periods and models considered.

Site no.	Spectral acceleration (T = 1 s) (*g*)								
	Return period : 475 years			Return period : 1000 years			Return period : 2475 years		
	Model 1	Model 2	Average	Model 1	Model 2	Average	Model 1	Model 2	Average
Site 1	0.50	1.35	1.25	0.68	1.74	1.71	0.95	2.33	1.98
Site 2	0.40	1.08	0.91	0.54	1.38	1.32	0.76	1.87	1.82
Site 3	0.51	1.36	1.27	0.69	1.76	1.72	0.96	2.34	1.98
Site 4	0.51	1.36	1.27	0.69	1.76	1.72	0.97	2.34	1.98
Site 5	0.48	1.29	1.15	0.65	1.66	1.66	0.92	2.21	1.95
Site 6	0.44	1.03	0.88	0.60	1.31	1.23	0.84	1.76	1.78
Site 7	0.44	1.05	0.90	0.60	1.34	1.28	0.85	1.80	1.80
Site 8	0.41	0.86	0.70	0.55	1.12	0.95	0.78	1.49	1.56
Site 9	0.39	0.88	0.72	0.53	1.13	0.96	0.76	1.52	1.59

energy radiated from the fault is conserved regardless of the selected subfault size. In this study, the dynamic corner frequency approach as implemented in the computer program EXSIM (Motazedian and Atkinson, 2005) is employed. In this approach, the acceleration spectrum $A_{ij}(f)$ of the ij^{th} subfault is expressed in terms of source, path, and site effects as follows:

$$A_{ij}(f) = C\, M_{0ij}\, H_{ij} \frac{(2\pi f)^2}{\left[1+\left(\frac{f}{fc_{ij}}\right)^2\right]} e^{-\frac{\pi f R_{ij}}{Q(f)\beta}} G\left(R_{ij}\right) D(f)\, e^{-\pi\kappa f}, \quad (6)$$

where $C = \frac{\Re^{\theta\varphi}\sqrt{2}}{4\pi\rho\beta^3}$ is a scaling factor, $\Re^{\theta\varphi}$ is the radiation pattern, ρ is the density, β is the shear-wave velocity, $M_{0_{ij}} = \frac{M_0 S_{ij}}{\sum_{k=1}^{nl}\sum_{l=1}^{nw} S_{kl}}$ is the seismic moment, S_{ij} is the relative slip weight, and $fc_{ij}(t)$ is the dynamic corner frequency of the ij^{th} subfault where the dynamic corner frequency $f_{c_{ij}}(t) = N_R(t)^{-1/3}\, 4.9 \times 10^6 \beta \left(\frac{\Delta\sigma}{M_{0ave}}\right)^{1/3}$. Here $\Delta\sigma$ is the stress drop, $N_R(t)$ is the cumulative number of ruptured subfaults at time t, and $M_{0_{ave}} = M_0 / N$ is the average seismic moment of subfaults. R_{ij} is the distance from the observation point, $Q(f)$ is the quality factor, $G(R_{ij})$ is the geometric spreading factor, $D(f)$ is the site amplification factor, and $e^{-\pi\kappa f}$ is a high-cut filter included to provide the spectral decay at high frequencies described with the κ factor of soils (Anderson and Hough, 1984). H_{ij} is a scaling factor introduced to conserve the high-frequency spectral level of the subfaults.

5.2. Input parameters of the DSHA

In this study, deterministic hazard analyses are performed for scenario earthquakes of magnitude Mw = 5.0, 5.5, 6.0, 6.5, and 7.0 on the same fault where the 13 March 1992 Erzincan event (Mw = 6.6) occurred (Figure 1). The 1992 Erzincan earthquake is also simulated. The location of that event's epicenter was critical in terms of its close distance to the city center. Thus, the epicenter of the earthquake is kept the same for all scenario events.

A total of 125 nodes are selected in the Erzincan region where full waveforms are simulated. Each node in the city center represents a small box of size 1 km × 1 km. The source and path parameters are selected according to Askan et al. (2013) where validation of these parameters is performed in terms of simulated and observed ground motion time histories of the 1992 Erzincan earthquake.

One of the most important parameters that affect the amplitude and frequency content of simulated waveforms is the site amplification factors. These factors are directly dependent on the wave velocity models at a site of interest. The results of wave velocity inversions of Section 3 are used in the simulations performed in this section. For each site, the velocity profile is employed to yield the corresponding local frequency-dependent site amplification factors. It is noted that a crustal velocity of 3700 m/s is defined as the bedrock velocity beneath the soil layers obtained from the joint MMSPAC and HVSR analyses.

All simulation parameters are displayed in Table 6.

Table 6. Input parameters used in the simulation of scenario earthquakes.

Parameter	Value
Hypocenter location	39°42.3 N, 39°35.2 E
Hypocenter depth	9 km
Depth to the top of the fault plane	2 km
Fault orientation	Strike: 125°, Dip: 90°
Fault dimensions	Wells and Coppersmith (1994)
Crustal shear wave velocity	3700 m/s
Rupture velocity	3000 m/s
Crustal density	2800 kg/m^3
Stress drop	Mohammadioun and Serva (2001)
Quality factor	Q = 122 f$^{0.68}$
Geometrical spreading	$R^{-1.1}$, $R \le 25$ km $R^{-0.5}$, $R > 25$ km
Duration model	T = T$_0$ + 0.05 R
Windowing function	Saragoni–Hart
Kappa factor	Regional kappa model (κ_0 = 0.066, Askan et al., 2013)
Site amplification factors	Amplifications based on local soil models expressed in Section 3

Table 7. Results of DSHA in terms of PGA for different scenario earthquakes.

Site no.	Vs30 (m/s)	Erzincan 1992		Mw = 5		Mw = 5.5		Mw = 6		Mw = 6.5		Mw = 7.0	
		R_{JB} (km)	PGA (*g*)	R_{JB} (km)	PGA (*g*)	R_{JB} (km)	PGA (*g*)	R_{JB} (km)	PGA (*g*)	R_{JB} (km)	PGA (*g*)	R_{JB} (km)	PGA (*g*)
1	262	7.31	0.46	9.76	0.05	10.92	0.1	8.57	0.17	7.31	0.39	3.76	0.67
2	483	3.28	0.73	11.01	0.03	11.17	0.13	7.54	0.25	3.28	0.46	0.27	1.2
3	248	6.17	0.55	10.09	0.05	10.94	0.08	8.09	0.33	6.17	0.35	2.62	0.58
4	247	5.52	0.66	10.23	0.04	10.92	0.12	7.85	0.19	5.52	0.47	1.97	1.24
5	297	4.43	0.56	10.8	0.03	11.21	0.09	7.79	0.22	4.43	0.39	0.88	0.85
6	368	5.91	0.55	15.13	0.03	15.48	0.05	11.92	0.14	5.91	0.37	2.37	0.66
7	362	5.73	0.5	14.63	0.02	14.99	0.07	11.44	0.21	5.73	0.3	2.18	0.61
8	460	4.41	0.31	12.93	0.03	13.18	0.06	9.57	0.18	4.41	0.43	0.86	0.99
9	474	4.3	0.42	12.38	0.03	12.65	0.1	9.06	0.18	4.3	0.46	0.75	0.76

Table 8. Results of DSHA in terms of SA (T = 0.2 s) for different scenario earthquakes.

Site no.	Vs30 (m/s)	Erzincan 1992		Mw = 5		Mw = 5.5		Mw = 6		Mw = 6.5		Mw = 7.0	
		R_{JB} (km)	SA (*g*) (T = 0.2 s)	R_{JB} (km)	SA (*g*) (T = 0.2 s)	R_{JB} (km)	SA (*g*) (T = 0.2 s)	R_{JB} (km)	SA (*g*) (T = 0.2 s)	R_{JB} (km)	SA (*g*) (T = 0.2 s)	R_{JB} (km)	SA (*g*) (T = 0.2 s)
1	262	7.31	1.28	9.76	0.12	10.92	0.23	8.57	0.46	7.31	0.81	3.76	1.76
2	483	3.28	1.62	11.01	0.06	11.17	0.39	7.54	0.54	3.28	1.18	0.27	2.85
3	248	6.17	1.54	10.09	0.13	10.94	0.32	8.09	0.52	6.17	1	2.62	1.87
4	247	5.52	1.09	10.23	0.07	10.92	0.18	7.85	0.35	5.52	0.66	1.97	1.5
5	297	4.43	1.34	10.8	0.07	11.21	0.16	7.79	0.41	4.43	1.15	0.88	2.27
6	368	5.91	1.06	15.13	0.08	15.48	0.15	11.92	0.38	5.91	0.76	2.37	1.7
7	362	5.73	0.98	14.63	0.06	14.99	0.14	11.44	0.41	5.73	1.04	2.18	1.91
8	460	4.41	0.63	12.93	0.08	13.18	0.22	9.57	0.32	4.41	0.84	0.86	1.8
9	474	4.3	1.05	12.38	0.09	12.65	0.23	9.06	0.43	4.3	1.14	0.75	1.62

Table 9. Results of DSHA in terms of SA (T = 1 s) for different scenario earthquakes.

Site no.	Vs30 (m/s)	Erzincan 1992		Mw = 5		Mw = 5.5		Mw = 6		Mw = 6.5		Mw = 7.0	
		R_{JB} (km)	SA (*g*) (T = 1 s)	R_{JB} (km)	SA (*g*) (T = 1 s)	R_{JB} (km)	SA (*g*) (T = 1 s)	R_{JB} (km)	SA (*g*) (T = 1 s)	R_{JB} (km)	SA (*g*) (T = 1 s)	R_{JB} (km)	SA (*g*) (T = 1 s)
1	262	7.31	0.78	9.76	0.04	10.92	0.09	8.57	0.14	7.31	0.53	3.76	0.99
2	483	3.28	0.58	11.01	0.02	11.17	0.05	7.54	0.14	3.28	0.29	0.27	0.56
3	248	6.17	0.39	10.09	0.04	10.94	0.04	8.09	0.23	6.17	0.84	2.62	0.84
4	247	5.52	0.57	10.23	0.03	10.92	0.1	7.85	0.37	5.52	0.85	1.97	0.56
5	297	4.43	0.44	10.8	0.04	11.21	0.04	7.79	0.11	4.43	0.47	0.88	0.45
6	368	5.91	0.78	15.13	0.02	15.48	0.06	11.92	0.17	5.91	0.27	2.37	0.51
7	362	5.73	0.38	14.63	0.02	14.99	0.09	11.44	0.24	5.73	0.3	2.18	0.95
8	460	4.41	0.49	12.93	0.01	13.18	0.02	9.57	0.13	4.41	0.3	0.86	0.67
9	474	4.3	0.34	12.38	0.01	12.65	0.05	9.06	0.14	4.3	0.21	0.75	0.82

5.3. Results of DSHA

The results of DSHA for Erzincan are obtained in the form a synthetic database composed of acceleration time series at the selected 125 grid points for the 1992 event as well as for each scenario earthquake. For space reasons, sample acceleration time series simulated for the scenario event of Mw = 7 are presented herein: Figure 27 displays the corresponding simulated accelerograms at the 9 sites where local soil models are derived. Then, to summarize the results of all scenario events, the ground motion amplitudes at the 9 sites of interest are presented: Tables 7–9 display the corresponding PGA, SA (T = 0.2 s), and SA (T = 1 s) at the sites for each scenario. It is observed that for all magnitude levels, sites with softer soils and close source-to-site distances (in terms of Joyner–Boore distance, R_{JB}) experience higher ground motion levels. For the Mw = 6.5 scenario, the maximum PGA reaches 0.5 *g* in the city center. For Mw = 7.0, the city center is subjected to PGA values exceeding 1 *g* at sites located close to the fault plane regardless of the soil conditions of that site (Site 2). Again, for the same scenario the PGA exceeds 1 *g* at sites with soft soil conditions (Site 4). When the spectral acceleration levels for T = 0.2 s are considered, it is observed that as the Mw of the earthquake gets larger, short R_{JB} distances govern the results rather than the site conditions. For the largest scenario earthquake with Mw = 7.0, the city center experiences very high spectral acceleration levels reaching 2 *g* at several locations. As stated previously, the city center is located on a basin of deep soft soil deposits. The soil medium is relatively stiffer in the northern regions; however, the fault plane is close to those nodes located in the north, which results in overall higher amplitudes at these locations. The SA (T = 1 s) values are also observed to be consistent with the previous observations, but with relatively lower amplitudes overall.

6. Discussion

In this study, 1D velocity models at 9 sites located in the Erzincan city center are derived using microtremor array analysis. The results are presented in terms of 1D soil velocity profiles as well as Vs30 values, which are incorporated into probabilistic and deterministic seismic hazard analyses performed for the city center. In addition, a ground motion simulation study for the 1992 Erzincan earthquake is also presented. Results are expressed in the form of PGA and spectral accelerations at the selected sites. These analyses constitute the first site-dependent detailed probabilistic and deterministic seismic hazard analyses for Erzincan in the literature. Locally derived input parameters for site response as well as seismic hazard analyses in this study yield numerical results that indicate the significant damage potential in Erzincan. Ground motion amplitudes obtained from site-specific deterministic hazard analyses

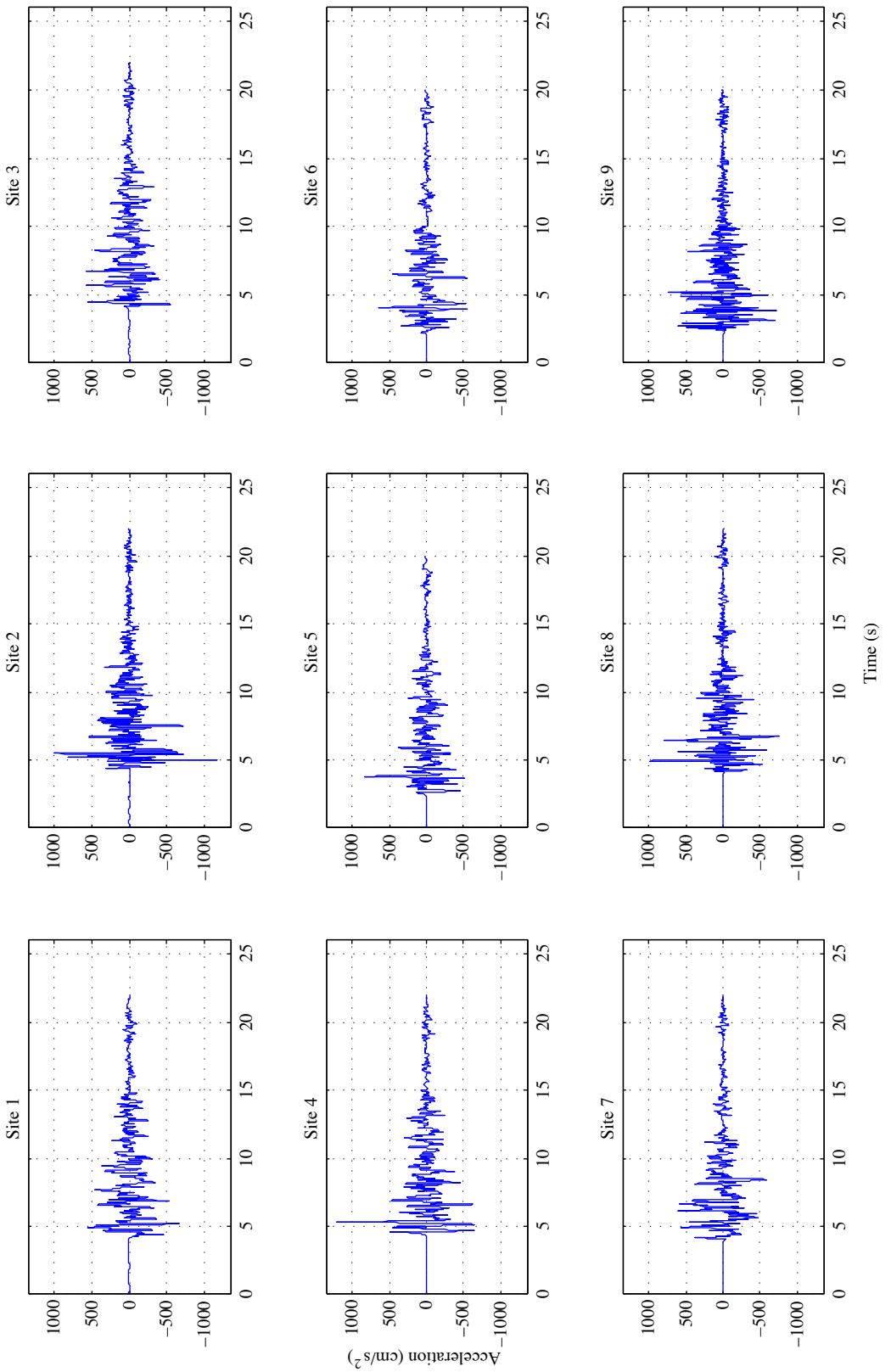

Figure 27. Simulated accelerograms at the 9 sites of interest for the scenario event of Mw = 7.

also explain the widespread structural damage observed during the 1992 Erzincan earthquake.

The wave velocity models in the north-south and east-west directions confirm the basin structure of the Erzincan city center. The southern parts are located on much softer soils while the northern sites involve relatively stiffer soil layers. The effect of local site conditions is more pronounced in the deterministic analysis than in the probabilistic one. This is because deterministic analysis considers soil amplification factors at each frequency to compute the ground motion levels at the sites, whereas in the probabilistic method only Vs30 is taken into account in calculation of GMPEs. In other words, DSHA yields a more site-specific ground motion distribution at different locations for a given scenario event. Finally, it is thought that the data and model uncertainties involved with the derivation of the soil models have a negligible effect on PSHA and DSHA results. Even though quantification of these sensitivities is out of scope herein, as long as the site class remains the same, such errors in soil models are not expected to have a significant effect on hazard results (Boore and Joyner, 1997; Askan et al., 2013, Asten et al., 2014).

When the results of PSHA are considered, the significant difference between two models that employ different sources is observed. The first one uses only area sources while the second one is a hybrid model that uses mostly line sources with few area sources. A comparison between these two source models shows that the use of only area sources clearly yields smaller hazard results. This is mainly because the activity rates are distributed over areas in area source models instead of those along the fault lines in line source models (Yılmaz-Öztürk, 2008; Yılmaz and Yücemen, 2015). Use of line sources is recommended in regions with well-defined active faults in close proximity.

Deterministic simulations reveal that the anticipated PGA levels in the city center during the 1992 event exceed 0.5 *g*, while the corresponding spectral accelerations at low periods (T = 0.2 s) exceed 1 *g*. This observation explains the widespread damage to the masonry buildings as well as low-rise reinforced concrete buildings in the city center during the earthquake despite the moderate magnitude (Sucuoglu and Tokyay, 1992).

In summary, all numerical results obtained with locally derived input parameters indicate that Erzincan has significant potential for hazard in terms of both local earthquake occurrence and site amplifications. Thus, a rapid evaluation of the existing buildings in the city in terms of their seismic capacities is required before another large event occurs, in order to avoid future economic and structural losses as well as fatalities.

Finally, the detailed results obtained in this study can be used for future applications in wave propagation studies; simulations for disaster planning, disaster mitigation, and rapid response; and estimation of insurance premiums in the Erzincan city center. The framework presented here can be employed for any other earthquake-prone region in our country as well as in the world.

Acknowledgments

This study was funded by the Turkish National Union of Geodesy and Geophysics project with project number TUJJB-UDP-01-12. Afet ve Acil Durum Yönetimi Başkanlığı (Disaster and Emergency Management Authority of Turkey, AFAD) and Dr Murat Nurlu in particular are acknowledged for provision of seismometers and team support in the field for the microtremor measurements.

References

Aki K (1957). Space and time spectra of stationary stochastic waves, with special reference to microtremors. B Earthq Res I Tokyo 35: 415–456.

Akinci A, Malagnini L, Herrmann RB, Pino NA, Scognamiglio L, Eyidogan H (2001). High-frequency ground motion in the Erzincan region, Turkey: Inferences from small earthquakes. B Seismol Soc Am 91: 1446–1455.

Aktar M, Dorbath C, Arpat E (2004). The seismic velocity and fault structure of the Erzincan Basin, Turkey, using local earthquake tomography. Geophys J Int 156: 497–505.

Anderson J, Hough SE (1984). A model for the shape of the Fourier amplitude spectrum of acceleration at high frequencies. B Seismol Soc Am 74: 1969–1993.

Arai H, Tokimatsu K (2004). S-wave velocity profiling by inversion of microtremor H/V spectrum. B Seismol Soc Am 94: 53–63.

Arai H, Tokimatsu K (2005). S-wave velocity profiling by joint inversion of microtremor dispersion curve and horizontal-to-vertical (H/V) spectrum. B Seismol Soc Am 95: 1766–1778.

Askan A, Sisman FN, Ugurhan B (2013). Stochastic strong ground motion simulations in sparsely-monitored regions: a validation and sensitivity study on the 13 March 1992 Erzincan (Turkey) earthquake. Soil Dyn Earthq Eng 55: 170–181.

Asten MW (2006). On bias and noise in passive seismic data from finite circular array data processed using SPAC methods. Geophysics 71: 153–162.

Asten MW (2009). Site shear velocity profile interpretation from microtremor array data by direct fitting of SPAC curves. In: Bard PY, Chaljub E, Cornou C, Cotton F, and Gueguen P, editors. Proceedings of the Third International Symposium on the Effects of Surface Geology on Seismic Motion (ESG2006), Vol. 2; Grenoble, France; 30 August–1 September 2006. Paris, France: LCPC, pp. 1069–1082.

Asten MW, Askan A, Ekincioglu EE, Sisman FN, Ugurhan B (2014). Site characterization in northwestern Turkey based on SPAC and HVSR analysis of microtremor noise. Explor Geophys 45: 74–85.

Asten MW, Dhu T, Lam N (2004). Optimized array design for microtremor array studies applied to site classification; observations, results and future use. In: Conference Proceedings of the 13th World Conference of Earthquake Engineering; 1–6 August 2004; Vancouver, Canada.

Barka A (1993). Tectonics of the Erzincan basin and its vicinity and 13 March 1992 Erzincan earthquake. In: Proceedings of the 2nd National Conference on Earthquake Engineering, pp. 259–70 (in Turkish with abstract in English).

Beresnev I, Atkinson GM (1997). Modeling finite-fault radiation from the wn spectrum. B Seismol Soc Am 87: 67–84.

Birgören G, Özel O, Siyahi B (2009). Bedrock depth mapping of southern coast of istanbul: comparison of analytical and experimental analyses. Turkish J Earth Sci 18: 315–329.

Bonnefoy-Claudet S, Cotton F, Bard PY (2006). The nature of noise wavefield and its applications for site effects studies: a literature review. Earth Sci Rev 79: 205–227.

Bonnefoy-Claudet S, Kohler A, Cornou C, Wathelet M, Bard PY (2008). Effects of Love waves on microtremor H/V ratio. B Seismol Soc Am 98**:** 288–300.

Boore DM, Atkinson GM (2008). Ground-motion prediction equations for the average horizontal component of PGA, PGV, and 5%-damped PSA at spectral periods between 0.01 s and 10.0 s. Earthq Spectra 24: 99–138.

Boore DM, Joyner WB (1997). Site amplifications for generic rock sites. B Seismol Soc Am 87: 327–341.

Castro RR, Pacor F, Franceschina G, Bindi D, Zonno G, Luzi L (2008). Stochastic strong-motion simulation of the Mw 6 Umbria– Marche earthquake of September 1997: Comparison of different approaches. B Seismol Soc Am 98: 662–670.

Cornell CA (1968). Engineering Seismic Risk Analysis. B Seismol Soc Am 58: 1583–1606.

Deniz A (2006). Estimation of earthquake insurance premium rates based on stochastic methods. MSc, Middle East Technical University, Ankara, Turkey.

Frankel A (1993). Three-dimensional simulations of the ground motions in the San Bernardino Valley, California, for hypothetical earthquakes on the San Andreas Fault. B Seismol Soc Am 83: 1020–1041.

Hayashi K, Nozu A, Tanaka M (2011). Joint inversion of three-component microtremor measurements and microtremor array measurements at Mexico City. In: SEG Technical Program Expanded Abstracts, pp. 917–921.

Ikeda T, Asten MW, Matsuoka T (2013). Joint inversion of spatial autocorrelation curves with HVSR for site characterization in Newcastle, Australia. In: 23rd ASEG International Geophysical Conference and Exhibition, Melbourne, Australia, Extended Abstracts, pp. 1–4.

Kalkan E, Gülkan P (2004). Site-dependent spectra derived from ground motion records in Turkey. Earthq Spectra 20: 1111–1138.

Kaypak B (2008). Three-dimensional VP and VP/VS structure of the upper-crust in the Erzincan basin (eastern Turkey). J Geophys Res 113: 1–20.

Kocaoğlu A, Fırtana K (2011). Estimation of shear wave velocity profiles by the inversion of spatial autocorrelation coefficients. J Seismol 15: 613–624.

Lav A, Erken A, İyisan R, Ansal A (1993). Erzincan'da yerel zemin koşulları ve yapısal hasar üzerindeki etkisi. In: Türkiye İnşaat Mühendisliği 12. Teknik Kongresi, Ankara, Turkey, pp. 25–39.

McGuire RK (2004). Seismic Hazard and Risk Analysis. Oakland, CA, USA: Earthquake Engineering Research Institute.

Mohammadioun B, Serva L (2001). Stress drop, slip type, earthquake magnitude, and seismic hazard. B Seismol Soc Am 91: 694–707.

Motazedian D, Atkinson GM (2005). Stochastic finite-fault modeling based on a dynamic corner frequency. B Seismol Soc Am 95: 995–1010.

Motazedian D, Moinfar A (2006). Hybrid stochastic finite fault modeling of 2003, M 6.5, Bam, earthquake (Iran). J Seismol 10: 91–103.

Okada H (2003). The Microtremor Survey Method. Geophysical Monograph Series No. 12. Tulsa, OK, USA: SEG.

Olsen KB, Archuleta RJ, Matarese JR (1996). Three-dimensional simulation of a magnitude 7.75 earthquake on the San Andreas Fault. Science 270: 1628–1632.

Picozzi M, Albarello D (2007). Combining genetic and linearized algorithms for a two-step joint inversion of Rayleigh wave dispersion and H/V spectral ratio curves. Geophys J Int 169: 189–200.

Power M, Chiou B, Abrahamson N, Bozorgnia Y, Shantz T, Roblee C (2008). An Overview of the NGA Project. Earthq Spectra 24: 3–21.

Richter CF (1958). Elementary Seismology, A Series of Books in Geology. 1st ed. San Francisco, CA, USA: W.H. Freeman and Co.

Roberts J, Asten MW (2004). Resolving a velocity inversion at the geotechnical scale using the microtremor (passive seismic) survey method. Explor Geophys 35: 14–18.

Schwartz DP, Coppersmith KJ (1984). Fault behavior and characteristic earthquakes: examples from the Wasatch and San Andreas Fault Zones. J Geophys Res 89: 5681–5698.

Sisman FN, Asten MW, Askan AA (2013). Determination of the site characterization properties in eastern segment of the North Anatolian Fault Zone in Turkey based on the MMSPAC method. In: Extended Abstracts of the 23rd ASEG Conference and Exhibition, pp. 1–4.

Sucuoglu H, Tokyay M (1992). 13 Mart 1992 Erzincan Depremi Mühendislik Raporu. Ankara, Turkey: İnşaat Mühendisleri Odası Ankara Şubesi (in Turkish).

Turkish Ministry of Public Works and Settlement (2007). Turkish Earthquake Code. Specification for Structures to be Built in Disaster Areas. Ankara, Turkey: Turkish Ministry of Public Works and Settlement.

Ugurhan B, Askan A (2010). Stochastic strong ground motion simulation of the 12 November 1999 Düzce (Turkey) earthquake using a dynamic corner. B Seismol Soc Am 100: 1498–1512.

Ugurhan B, Askan A, Akinci A, Malagnini L (2012). Strong-ground-motion simulation of the 6 April 2009 L'Aquila, Italy, earthquake. B Seismol Soc Am 102: 1429–1445.

Wathelet M, Jongmans D, Ohrnberger M (2005). Direct inversion of spatial autocorrelation curves with the neighborhood algorithm. B Seismol Soc Am 95: 1787–1800.

Wells DL, Coppersmith KJ (1994). New empirical relationships among magnitude, rupture length, rupture width, rupture area and surface displacement. B Seismol Soc Am 84: 974–1002.

Youngs RR, Coppersmith KJ (1985). Implications of fault slip rates and earthquake recurrence models to probabilistic seismic hazard estimates. B Seismol Soc Am 75: 939–964.

Yılmaz N, Yücemen MS (2015). Sensitivity of seismic hazard results to alternative seismic source and magnitude-recurrence models: a case study for Jordan. Geodin Acta 27: 189–202.

Yılmaz-Öztürk N (2008). Probabilistic seismic hazard analysis: a sensitivity study with respect to different models. PhD, Middle East Technical University, Ankara Turkey.

Yücemen MS (1982). Sismik Risk Analizi. Ankara, Turkey: Orta Doğu Teknik Üniversitesi (in Turkish).